EUROPEAN ORGANIZATION FOR NUCLEAR RESEARCH

ΛK femtoscopy in Pb–Pb collisions at $\sqrt{s_{\mathrm{NN}}} = 2.76$ TeV

ALICE Collaboration*

Abstract

The first measurements of the scattering parameters of ΛK pairs in all three charge combinations (ΛK^+, ΛK^-, and ΛK^0_S) are presented. The results are achieved through a femtoscopic analysis of ΛK correlations in Pb–Pb collisions at $\sqrt{s_{\mathrm{NN}}} = 2.76$ TeV recorded by ALICE at the LHC. The femtoscopic correlations result from strong final-state interactions, and are fit with a parametrization allowing for both the characterization of the pair emission source and the measurement of the scattering parameters for the particle pairs. Extensive studies with the THERMINATOR 2 event generator provide a good description of the non-femtoscopic background, which ~~result~~ results mainly from collective effects, with unprecedented precision. Furthermore, ~~this model~~ together with HIJING simulations ~~are~~, this model is used to account for contributions from residual correlations induced by feed-down from ~~resonances~~particle decays. The extracted scattering parameters indicate that the strong force is repulsive in the ΛK^+ interaction and attractive in the ΛK^- and ΛK^0_S interactions. The results suggest an effect arising either from different quark–antiquark interactions between the pairs ($s\bar{s}$ in ΛK^+ and $u\bar{u}$ in ΛK^-) ~~,~~or from different net strangeness for each system (S=0 for ΛK^+, and S=−2 for ΛK^-). Finally, the ΛK systems exhibit source radii larger than expected from extrapolation from identical particle femtoscopic studies. This effect is interpreted as resulting from the separation in space–time of the single-particle Λ and K source distributions.

*See Appendix D for the list of collaboration members

1 Introduction

Femtoscopy is an experimental method used to study the space–time characteristics of the particle emitting sources in relativistic particle collisions [1, 2]. With this method, two- (or many-) particle relative-momentum correlation functions are used to connect the final-state momentum distributions to the space–time distributions of particle emission at freeze-out. The correlation functions are sensitive to quantum statistics, as well as strong and Coulomb final-state interactions (FSI). Current femtoscopic studies are able to extract the size, shape, and orientation of the pair emission regions, as well as offer estimates of the total time to reach kinetic decoupling and the duration of particle emission [1, 3]. The momentum and species dependence of femtoscopic measurements affirms the collective nature of the hot and dense matter created in heavy-ion collisions [7–10]. Non-identical particle analyses additionally allow for the measurement of the space–time separation of the single particle source regions [4, 5, 7].

In addition to characterizing the source region, femtoscopy allows one to extract nuclear scattering parameters, many of which are difficult or impossible to measure otherwise. The subject of this analysis, ΛK pairs, interact only strongly; therefore, the studied femtoscopic signals are free from quantum statistical and Coulomb interaction effects. Calculations within Quantum Chromodynamics (QCD), the theory of the strong interaction, are notoriously difficult except in the regime of weak coupling, where perturbative methods may be applied. The ΛK analysis presented offers low energy QCD measurements, which fall into the non-perturbative regime of QCD. Therefore, the ΛK analysis not only gives insight into the strong interaction, it will also help guide future QCD calculations. Furthermore, the ΛK scattering parameters were not previously known, and theoretical predictions are limited. The extracted scattering parameters are compared to predictions obtained in the framework of chiral perturbation theory [11, 12]. Information about scattering parameters for similar systems are also very limited; past studies of kaon-proton scattering revealed the strong force is attractive in the K^-p interaction, and repulsive in that of the K^+p [13–15].

This paper presents the first measurements of the scattering parameters of ΛK pairs in all three charge combinations (ΛK^+, ΛK^-, and ΛK^0_S). The scattering parameters, along with pair emission source sizes, are extracted with a femtoscopic analysis of ΛK correlations in Pb–Pb collisions at $\sqrt{s_{NN}} = 2.76$ TeV measured by the ALICE experiment at the LHC. These correlations result from strong final-state interactions, and are fit with a parametrization by Lednický and Lyuboshitz [16]. Extensive studies with the THERMINATOR 2 event generator are performed to account for both non-femtoscopic backgrounds as well as contributions from residual correlations induced by feed-down from particle decays.

The organization of this paper is as follows. In Sec. 2 the data selection methods are briefly discussed. In Sec. 3 the analysis techniques utilized in this study are presented. Here, the two-particle correlation function is introduced, as well as the theoretical models with which the data are fit. This section also includes descriptions of the handling of residual correlations, corrections accounting for finite track momentum resolution, treatment of the non-femtoscopic background, as well as a brief description of the systematic uncertainties estimation. The final results are presented in Sec. 4 and concluding remarks are given in Sec. 5. Appendix A demonstrates an alternate approach to forming correlation functions, whose purpose here is to help eliminate the non-femtoscopic background. Appendix B discusses the procedure needed to generate fit functions when both the strong and Coulomb interactions are present. In Appendix C, the THERMINATOR 2 event generator is used to demonstrate the effect on a one-dimensional femtoscopic fit of a non-zero space-time separation between the single particle sources. Throughout the text, the pair name is used as shorthand

for the pair-conjugate system, which are found to be consistent (e.g., ΛK^+ for $\Lambda K^+ \oplus \overline{\Lambda} K^-$, ΛK^- for $\Lambda K^- \oplus \overline{\Lambda} K^+$, and ΛK^0_S for $\Lambda K^0_S \oplus \overline{\Lambda} K^0_S$), and ΛK is used to describe all ΛK combinations.

2 Data analysis

This work reports on the analysis of Pb–Pb collisions at $\sqrt{s_{NN}} = 2.76$ TeV produced by the LHC and measured by the ALICE experiment [17] in 2011. Approximately 40 million ~~combined central, semi-central, and minimum bias~~ events were analyzed~~. The events~~, which were classified according to their centrality percentiles determined using the measured amplitudes in the V0 detectors [18]. In order for an event to be included in the analysis, the ~~z~~ position of the reconstructed event vertex must be within 10 cm of the center of the ALICE detector ~~, and the event must contain at least one particle of each type from the pair of interest (e.g., for analysis, an accepted event must contain at least one and at least one)~~ along the beam axis.

Charged particle tracking was performed using the Time Projection Chamber (TPC) [19] and the Inner Tracking System (ITS) [20]. The ITS allows for high spatial resolution ~~in determining~~ of the primary (collision) vertex. The ~~determination of the momenta of the tracks was performed~~ momenta were determined by the tracking algorithm using tracks reconstructed with the TPC only and constrained to the primary vertex. Tracks were selected from the central pseudorapidity region, $|\eta| < 0.8$. A minimum requirement of 80 reconstructed TPC clusters was imposed, the purpose of which is to ensure both the quality of the track and good transverse momentum (p_T) resolution at large momenta, as well as to ~~remove~~ reject fake tracks.

Particle identification (PID) for reconstructed tracks was carried out using both the TPC and Time-Of-Flight (TOF) detectors [21, 22]~~in the pseudorapidity range $|\eta| < 0.8$~~. For TPC PID, a parametrized Bethe-Bloch formula was used to calculate the specific energy loss $\langle dE/dx \rangle$ in the detector expected for a particle with a given mass and momentum. For TOF PID, the particle mass was used to calculate the expected time of flight as a function of track length and momentum. For each PID method, a value (N_σ) was assigned to each track denoting the number of standard deviations between the measured track ~~information and calculated values~~ and the expected signal at a given momentum for a particular hypothesis particle species. This procedure was ~~repeated for four "particle species hypotheses"—~~ applied for each track assuming four different particle species hypotheses— electron, pion, kaon, and proton— ~~,~~ and for each hypothesis a different N_σ value was obtained per detector. These N_σ values were used to identify primary $K^\pm$ mesons, π and p daughters of Λ hyperons, and π daughters of K^0_S mesons, as well as to reject misidentified particles within each aforementioned sample.

2.1 $K^\pm$ selection

The single-particle selection criteria used to select charged kaon candidates are summarized in Table 1. Track reconstruction for the charged kaons was performed using the TPC, and tracks within the range $0.14 < p_T < 1.5$ GeV/c were accepted for analysis. To reduce the number of secondary particles (e.g., charged particles produced in the detector material, particles from weak decays, etc.) in the sample, a selection criterion is established based on the maximum distance-of-closest-approach (DCA) of the track to the primary vertex. This is realized by imposing a restriction on the DCA in both the transverse and beam directions.

Particle identification was performed using both the TPC and TOF detectors via the N_σ method. The N_σ selection criteria become tighter with increasing momentum to reduce contamination within the samples, as the $K^\pm$ signals begin to overlap more significantly with those from other particles, particularly $e^\pm$ and $\pi^\pm$. ~~Additional methods~~ $\pi^\pm$. Rejection procedures are included to reduce the contamination in the $K^\pm$ samples from ~~the~~ electrons and pions. The specifics for the $K^\pm$ selection are contained in Table 1. The purity of the $K^\pm$ collections, $P_{K^\pm}$, was estimated to be approximately 97% from a Monte-Carlo (MC)

115 study based on HIJING [23] simulations using GEANT3 [24] to model particle transport through the
116 ALICE detectors. For a more detailed estimate of the $K^\pm$ purity from an analysis employing similar
117 methods, see [25].

Table 1: Selection criteria for $K^\pm$ mesons

$K^\pm$ selection	
Transverse momentum p_T	$0.14 < p_T < 1.5$ GeV/c
$\|\eta\|$	< 0.8
Transverse DCA to primary vertex	< 2.4 cm
Longitudinal DCA to primary vertex	< 3.0 cm
TPC and TOF N_σ	
$\quad p < 0.4$ GeV/c	$N_{\sigma K,TPC} < 2$
$\quad 0.4 \le p < 0.45$ GeV/c	$N_{\sigma K,TPC} < 1$
$\quad 0.45 \le p < 0.80$ GeV/c	$N_{\sigma K,TPC} < 3$ $N_{\sigma K,TOF} < 2$
$\quad 0.80 \le p < 1.0$ GeV/c	$N_{\sigma K,TPC} < 3$ $N_{\sigma K,TOF} < 1.5$
$\quad p \ge 1.0$ GeV/c	$N_{\sigma K,TPC} < 3$ $N_{\sigma K,TOF} < 1$
Electron rejection: reject if all satisfied	~~$N_{\sigma e^-,TPC} <$~~ $N_{\sigma e,TPC} \lesssim 3$ ~~$N_{\sigma e^-,TPC} < N_{\sigma K^\pm,TPC}$~~ $N_{\sigma e,TPC} \lesssim N_{\sigma K,TPC}$ ~~$N_{\sigma e^-,TOF} < N_{\sigma K^\pm,TOF}$~~ $N_{\sigma e,TOF} \lesssim N_{\sigma K,TOF}$
Pion rejection: reject if:	

Pion rejection: reject if:			
$p < 0.65$ GeV/c	TOF and TPC available		~~$N_{\sigma\pi,TPC} <$~~ $N_{\sigma\pi,TPC} \lesssim 3$ ~~$N_{\sigma\pi,TOF} <$~~ $N_{\sigma\pi,TOF} \lesssim 3$
	Only TPC available	$p < 0.5$ GeV/c	~~$N_{\sigma\pi,TPC} <$~~ $N_{\sigma\pi,TPC} \lesssim 3$
		$0.5 \le p < 0.65$ GeV/c	~~$N_{\sigma\pi,TPC} <$~~ $N_{\sigma\pi,TPC} \lesssim 2$
$0.65 \le p < 1.5$ GeV/c			~~$N_{\sigma\pi,TPC} <$~~ $N_{\sigma\pi,TPC} \lesssim 5$ ~~$N_{\sigma\pi,TOF} <$~~ $N_{\sigma\pi,TOF} \lesssim 3$
$p \ge 1.5$ GeV/c			~~$N_{\sigma\pi,TPC} <$~~ $N_{\sigma\pi,TPC} \lesssim 5$ ~~$N_{\sigma\pi,TOF} <$~~ $N_{\sigma\pi,TOF} \lesssim 2$

118 2.2 K^0_S and Λ selection

119 Electrically neutral Λ ($\overline{\Lambda}$) and K^0_S particles are reconstructed through their weak decays: $\Lambda \to p$~~π^-~~ π^-
120 ($\overline{\Lambda} \to$ ~~$\pi^+\overline{p} \to$~~ $\pi^+\overline{p}$) and $K^0_S \to$ ~~$\pi^+\pi^-$~~ $\pi^+\pi^-$, with branching ratios 63.9% and 69.2% [26], respectively.
121 The obtained candidates are denominated as V^0 particles ~~. The main~~ due to their decay topology. The
122 selection criteria used are shown in Tables 2 and 3. Aside from ~~typical~~ kinematic and PID selection
123 methods (using TPC and TOF detectors), the tracks of the decay products (called *daughters*) ~~are also~~
124 ~~exposed to~~ must also meet a minimum requirement ~~of~~ on their impact parameter with respect to the
125 primary vertex. The decay vertex of the V^0 is ~~assumed to be the point of closest approach between the~~
126 ~~daughter tracks~~ calculated based on the positions in which the two daughter tracks were closest. To help
127 ~~ensure quality~~ in reducing combinatorial background, a maximum value is demanded on the distance
128 of closest approach between the daughters (DCA V^0~~Daughters~~daughters). The positive and negative
129 daughter tracks are combined to form the V^0 candidate, the momentum of which is the sum of the
130 momenta of the daughters ~~(calculated at the DCA)~~calculated in the condition in which they were closest
131 to one another.

132 To select primary candidates, the impact parameter with respect to the primary vertex is used as a selec-
133 tion criterion for each V^0. Furthermore, a restriction is imposed on the pointing angle, θ_{PA}, between the

134 V^0 momentum and the vector pointing from the primary vertex to the secondary V^0 decay vertex, which
135 is achieved by appointing a minimum value on $\cos(\theta_{PA})$ ("Cosine of pointing angle" in Tables 2 and 3).

136 In order to remove the contamination to the Λ ($\overline{\Lambda}$) and K_S^0 samples due to misidentification of the protons
137 and pions for each V^0, the mass assuming different identities (Λ, $\overline{\Lambda}$, and K_S^0 hypotheses) is calculated
138 and utilized in a misidentification procedure. The K_S^0 hypothesis ($m_{\text{inv, }K_S^0\text{ hyp.}}$) is calculated assuming
139 ~~$\pi^\pm\pi^\mp$~~ $\pi^+\pi^-$ daughters, the Λ hypothesis ($m_{\text{inv, }\Lambda\text{ hyp.}}$) assumes p~~π^-~~ π^- daughters, and the $\overline{\Lambda}$ hypothesis
140 ($m_{\text{inv, }\overline{\Lambda}\text{ hyp.}}$) assumes ~~$\overline{p}\pi^\pm$~~ $\overline{p}\pi^+$ daughters. In the misidentification methods, the calculated masses are
141 compared to the corresponding particle masses of the K_S^0 and Λ ($\overline{\Lambda}$), $m_{\text{PDG,}K_S^0}$ and $m_{\text{PDG,}\Lambda(\overline{\Lambda})}$ respec-
142 tively, as recorded by the Particle Data Group [26]. For Λ ($\overline{\Lambda}$) selection, a candidate is concluded to be
143 misidentified and is rejected if all of the following criteria are satisfied:

144 1. $\left| m_{\text{inv, }K_S^0\text{ hyp.}} - m_{\text{PDG, }K_S^0} \right| < 9.0 \text{ MeV}/c^2$,

145 2. daughter particles pass daughter selection criteria intended for K_S^0 reconstruction,

146 3. $\left| m_{\text{inv, }K_S^0\text{ hyp.}} - m_{\text{PDG, }K_S^0} \right| < \left| m_{\text{inv, }\Lambda(\overline{\Lambda})\text{ hyp.}} - m_{\text{PDG, }\Lambda(\overline{\Lambda})} \right|$.

147 Similarly, for K_S^0 selection, a candidate is rejected if all of the following criteria are satisfied for the Λ
148 case, or for the $\overline{\Lambda}$ case:

149 1. $\left| m_{\text{inv, }\Lambda(\overline{\Lambda})\text{ hyp.}} - m_{\text{PDG, }\Lambda(\overline{\Lambda})} \right| < 9.0 \text{ MeV}/c^2$,

150 2. daughter particles pass daughter selection criteria intended for Λ ($\overline{\Lambda}$) reconstruction,

151 3. $\left| m_{\text{inv, }\Lambda(\overline{\Lambda})\text{ hyp.}} - m_{\text{PDG, }\Lambda(\overline{\Lambda})} \right| < \left| m_{\text{inv, }K_S^0\text{ hyp.}} - m_{\text{PDG, }K_S^0} \right|$.

152 A final restriction on the invariant mass (m_{inv}) is applied to enhance the purity. These selection criteria
153 are shown in Tables 2 and 3. To avoid any auto-correlation effects, all V^0 candidates within each single-
154 particle collection (Λ, $\overline{\Lambda}$, and K_S^0 separately) are ensured to have unique daughters. If a daughter is
155 found to be shared among V^0 candidates in a given collection, only that with the smallest DCA to the
156 primary vertex is kept. This procedure ensures unique single-particle collections before particle pairs
157 are constructed; the elimination of shared daughters between the particles within each pair is described
158 below in Sec. 2.3. The resulting invariant mass distributions for Λ and K_S^0 collections in the 0–10%
159 centrality interval are shown in Fig. 1. For the purity estimations, the background signal is ~~estimated~~
160 extracted by fitting the m_{inv} distribution with a fourth-order polynomial outside of the mass peak and
161 assuming the distribution to continue smoothly ~~within~~ beneath the mass peak. The Λ and $\overline{\Lambda}$ purities are
162 estimated to be ~~$P_{\Lambda(\Lambda)} \approx 95\%$~~ $P_{\Lambda(\overline{\Lambda})} \approx 96\%$, and that of the K_S^0 is $P_{K_S^0} \approx 98\%$.

2.3 Pair construction

164 In order to reduce the contamination to the two-particle correlations due to pairs sharing daughters~~and~~
165 ~~to split or merged tracks~~, track splitting (two tracks reconstructed from one particle), and track merging
166 (one track reconstructed from two particles), two main pair rejection procedures are applied: a shared
167 daughter restriction, and an average separation constraint. The purpose of the shared daughter restriction
168 is to ensure the first particle in the pair is unique from the second. For pairs formed of two V^0s (i.e.,
169 ΛK_S^0), this is implemented by removing all pairs which share a daughter. For a pair formed of a single
170 V^0 and a charged track (i.e., $\Lambda K^\pm$), the restriction removes all pairs in which the charged track is also
171 claimed as a daughter of the V^0.

Table 2: Selection criteria for Λ and $\overline{\Lambda}$ hyperons

Λ [$\overline{\Lambda}$] selection	
Transverse momentum p_T	> 0.4 GeV/c
$|\eta|$	< 0.8
Invariant mass	$|m_{p\pi} - m_{PDG}| < 3.8$ MeV/c^2
DCA to primary vertex	< 0.5 cm
Cosine of pointing angle	> 0.9993
Decay length	< 60 cm
π and p daughter criteria	
$|\eta|$	< 0.8
DCA πp daughters	< 0.4 cm
π-specific	
p_T	> 0.16 GeV/c
DCA to primary vertex	> 0.3 cm
TPC and TOF N_σ	

TPC and TOF N_σ		
$p < 0.5$ GeV/c		$N_{\sigma,TPC} < 3$
$p \geq 0.5$ GeV/c	TOF & TPC available	$N_{\sigma,TPC} < 3$ $N_{\sigma,TOF} < 3$
	Only TPC available	$N_{\sigma,TPC} < 3$

p-specific		
p_T		> 0.5(p) [0.3($\overline{p}$)] GeV/c
DCA to primary vertex		> 0.1 cm
TPC and TOF N_σ		
$p < 0.8$ GeV/c		$N_{\sigma,TPC} < 3$
$p \geq 0.8$ GeV/c	TOF & TPC available	$N_{\sigma,TPC} < 3$ $N_{\sigma,TOF} < 3$
	Only TPC available	$N_{\sigma,TPC} < 3$

Table 3: Selection criteria for K_S^0 mesons

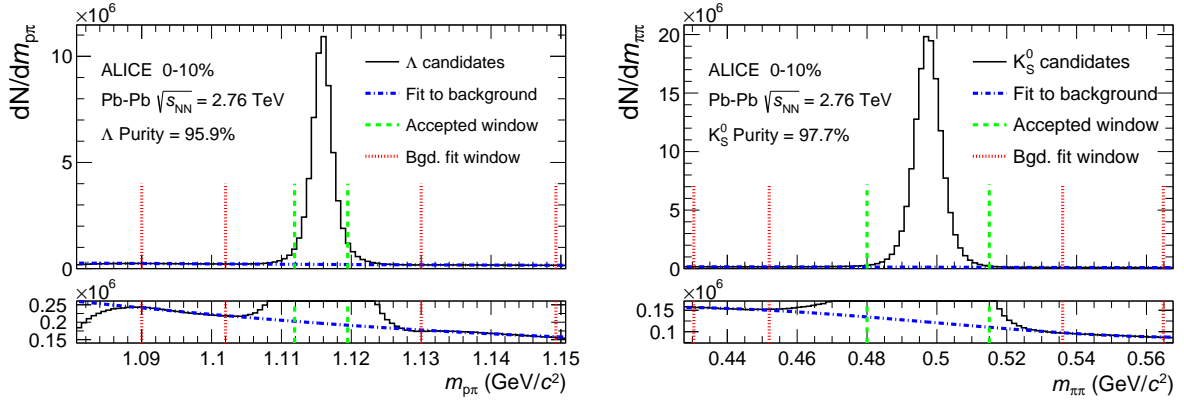| K_S^0 selection		
Transverse momentum p_T		> 0.2 GeV/c
$|\eta|$		< 0.8
Invariant mass		$0.480 < m_{\pi^+\pi^-} < 0.515$ GeV/c^2
DCA to primary vertex		< 0.3 cm
Cosine of pointing angle		> 0.9993
Decay length		< 30 cm
$\pi^\pm$ daughter criteria		
p_T		> 0.15 GeV/c
$|\eta|$		< 0.8
DCA $\pi^+\pi^-$ daughters		< 0.3 cm
DCA to primary vertex		> 0.3 cm
TPC and TOF N_σ		
$p < 0.5$ GeV/c		$N_{\sigma,TPC} < 3$
$p \geq 0.5$ GeV/c	TOF & TPC available	$N_{\sigma,TPC} < 3$ $N_{\sigma,TOF} < 3$
	Only TPC available	$N_{\sigma,TPC} < 3$

Figure 1: (Color online) Invariant mass ~~() distribution~~ distributions in the 0–10% centrality interval of (a) p$\pi^+\pi^-$ pairs showing the Λ peak, and of (b) ~~$\pi^+\pi^-$~~ $\pi^+\pi^-$ pairs showing the K_S^0 peak, for V^0 candidates. The bottom panels are zoomed to show the background with fit. The vertical dashed (green) lines represent the selection restrictions used in the analyses, the vertical dotted (red) lines delineate the region over which the background was fit, and the dash-dotted (blue) line shows the background fit.

The purpose of the average separation constraint is to remove splitting and merging effects, and it is employed in the following way. The average separation between two tracks is calculated using their spatial separation as determined at several points throughout the TPC (every 20 cm radially from 85 cm to 245 cm). For the ΛK_S^0 analysis, which involves two V^0 particles, a minimum average separation constraint of 6 cm between the like-charge daughters in the pairs is imposed (for example, between the p daughter of the Λ and the ~~π^+~~ π^+ daughter of the K_S^0). For the $\Lambda K^\pm$ analyses, a minimum average separation constraint of 8 cm is enforced between the $K^\pm$ and the Λ daughter sharing the same charge (for example, in the ΛK^+ analysis, between the p daughter of the Λ and the K^+). ~~The constraint values used coincide with the values at which the average separation correlation functions stabilize to unity, signifying the splitting~~ Splitting and merging effects ~~are no longer abundant. These effects~~ between oppositely charged tracks were found to be negligible, therefore no constraints on unlike-charge tracks are imposed.

3 Analysis methods

3.1 Correlation function

The ~~two-particle~~ correlation function for particles a and b, ~~$C_{ab}(\vec{p}_a, \vec{p}_b)$~~ $C_{ab}(\mathbf{p}_a, \mathbf{p}_b)$, is defined as the ratio of the probability of simultaneously measuring two particles with momenta ~~p_a and p_b~~ $\mathbf{p}_a$ and $\mathbf{p}_b$, to the product of the single-particle probabilities. These probabilities are directly related to the covariant two-particle spectrum, ~~$E_a E_b \frac{dN_{ab}}{d^3 p_a d^3 p_b}$~~ $E_a E_b \frac{d^6 N_{ab}}{d^3 p_a d^3 p_b}$, and the single-particle spectra, ~~$E_{a(b)} \frac{dN_{a(b)}}{d^3 p_{a(b)}}$~~ $E_{a(b)} \frac{d^3 N_{a(b)}}{d^3 p_{a(b)}}$, and the correlation function may be written

$$C_{ab}(\mathbf{p}_a, \mathbf{p}_b) = \frac{E_a E_b \frac{d^6 N_{ab}}{d^3 p_a d^3 p_b}}{\left(E_a \frac{d^3 N_a}{d^3 p_a} \right) \left(E_b \frac{d^3 N_b}{d^3 p_b} \right)}, \tag{1}$$

where N_{ab} is the yield of particle pairs, $E_{a(b)}$ is the energy, $p_{a(b)}$ is the three-momentum, and $N_{a(b)}$ is the yield of particles $a(b)$. Theoretically, the correlation function may be expressed as in the Koonin-Pratt equation [27, 28],

$$C(\mathbf{k}^*) = \int S_\mathbf{P}(\mathbf{r}^*) |\Psi_{\mathbf{k}^*}(\mathbf{r}^*)|^2 d^3 \mathbf{r}^*, \tag{2}$$

194 where $\mathbf{k}^*$ is the relative momentum of the pair (defined as ~~$\mathbf{k}^* = \frac{1}{2}|\mathbf{p}_1^* - \mathbf{p}_2^*|$, where $\mathbf{p}_1^*$ and $\mathbf{p}_2^*$~~ $\mathbf{k}^* = \frac{1}{2}|\mathbf{p}_a^* - \mathbf{p}_b^*|$,
195 where $\mathbf{p}_a^*$ and $\mathbf{p}_b^*$ are the momenta of the two particles) in the pair rest frame (PRF, denoted with an
196 asterisk *), $\mathbf{r}^*$ is the relative separation in the same frame, $\mathbf{P}$ is the total pair momentum, $S_{\mathbf{P}}(\mathbf{r}^*)$ is the
197 pair source distribution, and $\Psi_{\mathbf{k}^*}(\mathbf{r}^*)$ is the two-particle wave-function. ~~Within the $|\Psi|^2$ term the particle~~
198 ~~interaction information is contained, and therefore the scattering parameters.~~

199 In practice, the correlation function is formed experimentally as

$$C(k^*) = \mathcal{N}\frac{A(k^*)}{B(k^*)}, \tag{3}$$

200 where $A(k^*)$ is the signal distribution, $B(k^*)$ is the reference distribution, and $\mathcal{N}$ is a normalization
201 parameter. The reference distribution is used to divide out the phase-space effects, leaving only the
202 ~~femtoscopic~~ physical effects in the correlation function. The normalization parameter is chosen such
203 that the mean value of the correlation function equals unity for $k^* \in [0.32, 0.4]$ GeV/c. The signal
204 distribution is the same-event distribution of particle pairs. ~~Typically~~The reference distribution, $B(k^*)$,
205 is obtained using mixed-event pairs [29], i.e., particles from a given event are paired with those from
206 another event. ~~Other techniques exist; most notably, one may use same-event pairs after rotating one~~
207 ~~particle in the pair by 180° in the transverse plane (see Sec. 3.5 and App. A for more details).~~ For this
208 analysis, ~~the typical mixed-event method is utilized, and~~ each event is ~~mixed~~ combined with five others
209 for the reference distribution construction. To be included in the mixing pool, an event must contain
210 at least one particle of each type from the pair of interest (e.g., for the $\Lambda\mathrm{K}^0_\mathrm{S}$ analysis, an accepted event
211 must contain at least one Λ and at least one K^0_S). In order to mix similar events, only ~~events~~ those of like
212 centrality (within 5%) and of like primary vertex position (within 2 cm) are ~~mixed~~combined.

213 This analysis presents correlation functions for three centrality percentile ranges (0–10%, 10–30%,
214 and 30–50%), and is integrated in pair transverse momentum ($k_\mathrm{T} = \frac{1}{2}|\mathbf{p}_{\mathrm{T},1} + \mathbf{p}_{\mathrm{T},2}|$) ~~integrated (i.e., no~~
215 ~~restriction on k_T)~~ due to limited data. The k_T dependences of the three $\Lambda\mathrm{K}$ charge combinations should
216 be comparable, so an integrated analysis is acceptable. ~~The correlation functions were constructed~~
217 ~~separately for the two different field polarities applied by the ALICE L3 solenoid magnet during the~~
218 ~~data acquisition. These are kept separate during the fitting process, and are combined using a weighted~~
219 ~~average when plotting, where the weight is the number of numerator pairs in the normalization range.~~

3.2 Modeling the correlation function

221 In the absence of the Coulomb interaction, the correlation function can be described analytically with a
222 model derived by Lednický and Lyuboshitz [16]. Within the model, the (non-symmetrized) two-particle
223 wave function is expressed as a superposition of a plane wave and diverging spherical wave, and the
224 complex scattering amplitude, $f^S(k^*)$, is evaluated via the effective range approximation,

$$f^S(k^*) = \left(\frac{1}{f_0^S} + \frac{1}{2}d_0^S k^{*2} - ik^*\right)^{-1}, \tag{4}$$

225 where f_0^S is the complex s-wave scattering length, d_0^S is the effective range of the interaction, and S
226 denotes the total spin of the particular pair. The sign convention is such that a positive real component
227 of the scattering length, $\Re f_0$, represents an attractive interaction, while a negative $\Re f_0$ ~~value~~ represents
228 a repulsion. A spherically symmetric Gaussian distribution with radius R_inv is assumed for the pair
229 emission source in the PRF. With these assumptions, utilizing the Koonin-Pratt equation (Eq. ~~2~~(2)),
230 the correlation function for non-identical particle pairs ~~with at least one uncharged member is given~~ is

231 modeled by [16]

$$
C(k^*)_{\text{Lednický}} = 1 + \sum_S \rho_S \left[\frac{1}{2} \left| \frac{f^S(k^*)}{R_{\text{inv}}} \right|^2 \left(1 - \frac{d_0^S}{2\sqrt{\pi}R_{\text{inv}}} \right) \right.
$$
$$
\left. + \frac{2\Re f^S(k^*)}{\sqrt{\pi}R_{\text{inv}}} F_1(2k^*R_{\text{inv}}) - \frac{\Im f^S(k^*)}{R_{\text{inv}}} F_2(2k^*R_{\text{inv}}) \right],
$$
(5)

232 where $\Re f^S(k^*)$ and $\Im f^S(k^*)$ denote the real and imaginary parts of the complex scattering length, re-
233 spectively, and F_1 and F_2 are ~~the analytic functions~~ analytic functions [16]. The weight factor, ρ_S, is the
234 normalized emission probability for a state of total spin S; in the assumed case of unpolarized emission,
235 $\rho_S = (2S+1)/[(2j_1+1)(2j_2+1)]$, where $j_{1,2}$ are the spins of the particles in the pair. The Λ hyperon
236 is spin-1/2 and K mesons are spin-0, so the ΛK system only has one possible total spin state S, and
237 therefore $C(k^*)$ in Eq. ~~5~~ (5) has only a single term. In the following, the S superscript is dropped from
238 all scattering parameters.

3.3 Residual correlations

240 The purpose of this analysis is to study the interaction and scale of the emitting source of the primary
241 ΛK pairs. However, in practice some of the selected particles originate as ~~decay~~ products from other
242 ~~resonances~~ decaying particles after kinetic freeze-out (secondary particles), and some of the final pairs
243 contain a misidentified member. In both cases, these contribute to the ~~finally~~ observed correlation func-
244 tion, and obscure its relation to the primary ΛK system. The ~~contributions~~ net contribution from fake
245 pairs, which contain at least one misidentified member, ~~are assumed~~ is taken to average to unity, in
246 which case they simply attenuate the femtoscopic signal. Pairs ~~whose members originate as daughters~~
247 ~~from resonances~~ in which at least one member originates from a particle decay (e.g., ΛK$^+$ from Σ^0K$^+$)
248 carry information about the parent system. In effect, the correlation between the parents will be visible,
249 although smeared out, in the daughters' signal. This is termed a residual correlation resulting from feed-
250 down. As described in the following, the main sources of residual correlations in the ΛK systems result
251 from Λ hyperons which have ~~decayed~~ been produced from Σ^0, Ξ^0, and Ξ^- ~~parents~~ decays.

252 The ~~finally~~ measured correlation function is a combination of the genuine ΛK correlation with contribu-
253 tions from ~~resonances~~ particle decays and impurities [30],

$$
C_{\text{measured}}(k^*_{\Lambda K}) = 1 + \sum_{ij} \lambda'_{ij}[C_{ij}(k^*_{\Lambda K}) - 1],
$$
(6)

254 with

$$
\lambda'_{ij} = \lambda_{\text{Fit}}\lambda_{ij},
$$
$$
\sum_{ij} \lambda'_{ij} = \lambda_{\text{Fit}} \sum_{ij} \lambda_{ij} = \lambda_{\text{Fit}},
$$
(7)

255 where the ~~term represents the genuine correlation, and the~~ ij terms ~~denote~~ include the primary ΛK contribution
256 together with the contributions from residual feed-down and impurities. More specifically, $C_{ij}(k^*_{\Lambda K})$ is
257 the correlation function of the parent system expressed in terms of the relative momentum of the daughter
258 ΛK pair. The λ_{ij} parameters serve as weights dictating the relative strength of each component's con-
259 tribution to the observed signal, and are normalized to unity (i.e., $\sum_{ij} \lambda_{ij} = 1$, where ij includes also the
260 primary ΛK component) [30, 31]. ~~The~~ When the experimental correlation functions are fit, the individual
261 λ_{ij} are fixed (and whose values can be found in Table 4), but the parameter λ_{Fit} in Eq. ~~6~~ (6) is left free.

262 To ~~obtain~~ model the parent correlation function expressed in the relative momentum of the daughter pair,

a transform matrix is utilized,

$$C_{ij}(k^*_{\Lambda K}) \equiv \frac{\sum\limits_{k^*_{ij}} C_{ij}\left(k^*_{ij}\right) T\left(k^*_{ij}, k^*_{\Lambda K}\right)}{\sum\limits_{k^*_{ij}} T\left(k^*_{ij}, k^*_{\Lambda K}\right)},$$ (8)

where $T(k^*_{ij}, k^*_{\Lambda K})$ is the transform matrix, which is generated with the THERMINATOR 2 [32] simulation. The transform matrix describes the decay kinematics of the parent system into the daughter system, and is essentially an unnormalized probability distribution mapping the k^* of the parent pair to that of the daughter pair when one or both parents decay (see [30] for more details).

The contribution of a parent system (e.g., $\Sigma^0 K^+$) to the daughter correlation function (e.g., ΛK^+) in the fit procedure is determined by modeling the parent system's correlation function and running it through the appropriate transform matrix. Since the interactions between these particles are not known, some assumptions must be made. When modeling the parent systems, the source radii are assumed to be equal to those of the daughter ΛK systems. Furthermore, Coulomb-neutral parent pairs are assumed to share the same scattering parameters as the ΛK daughter pair, and the parent correlation function is modeled using Eq. (5). During the fit process, these source radii and scattering parameters are left free, as described in Sec. 3.6. For the $\Xi^- K^\pm$ parent system, where the constituents interact via both the strong and Coulomb interactions, no analytical expression exists to model the correlation function (see App. B), and the experimental $\Xi^- K^\pm$ data are used. However, the $\Xi^- K^\pm$ correlation function is dominated by the contribution from the Coulomb interaction, and may be sufficiently modeled with a Coulomb-only scenario (in which the strong interaction is assumed to be negligible) for this analysis, to yield consistent results.

The λ_{ij} parameters dictate the relative strength of each contribution to the correlation function, and can be estimated using the THERMINATOR 2 and HIJING simulations. More specifically, a λ_{ij} parameter is estimated as the total number of ΛK pairs in the sample originating from source ij (N_{ij}) divided by the total number of ΛK pairs. For a given ΛK source, the number of detected pairs depends on both the raw yield and the reconstruction efficiency. The relevant reconstruction efficiencies are those of the daughters under study, not of the parent particles; e.g., when determining the contribution of the $\Xi^- K^+$ system to the ΛK^+ correlation function, the reconstruction efficiency of the Ξ^- is not relevant, but that of the secondary Λ originating from a Ξ^- decay is. The reconstruction efficiencies (RE_{ij}) are estimated with HIJING simulations using GEANT3 to model particle transport through the detector. HIJING events are generated from a superposition of PYTHIA pp collisions, and lack the strangeness saturation of a fully thermalized medium. As a result, HIJING is unreliable in providing the yields needed for this analysis, and, instead, the yields are estimated with the THERMINATOR 2 simulation (N^{THERM}_{ij}). The number of ΛK pairs from source ij is then estimated as the product of the yield with the associated reconstruction efficiency, $N_{ij} \equiv N^{\mathrm{THERM}}_{ij} RE^{\mathrm{HIJING}}_{ij}$. Finally, the λ_{ij} are estimated as

$$\lambda_{ij} = \frac{N_{ij}}{N_{\mathrm{Total}}} = \frac{N^{\mathrm{THERM}}_{ij} RE^{\mathrm{HIJING}}_{ij}}{\sum\limits_{\alpha\beta} N^{\mathrm{THERM}}_{\alpha\beta} RE^{\mathrm{HIJING}}_{\alpha\beta}}.$$ (9)

Femtoscopic analyses are sensitive to the pair emission structure at kinetic freeze-out. Therefore, within femtoscopy, any particle which originates from a particle decay before last rescattering is considered primary. The THERMINATOR 2 simulation shows that the Λ hyperons and K mesons decay from a large number of particle species ($\sim$50 Λ parent species, and $\sim$70 K parent species), and the most significant contributing pair systems are $\Sigma^0 K$, $\Xi^- K$, $\Xi^0 K$, $\Sigma^{*+} K$, $\Sigma^{*-} K$,

Σ^{*0}K, ΛK*, Σ^0K*, Ξ^-K*, and Ξ^0K*. However, the simulation does not include a hadronic rescattering phase, and not all of the aforementioned pair systems will survive until kinetic freeze-out. The systems resulting from electromagnetic or weak decays (Σ^0, Ξ^-, and Ξ^0) will survive long after kinetic freeze-out, and will contribute residual signals to the ΛK correlation functions. The majority of the remaining contributors decay via the strong interaction with mean proper lifetimes less than a few fm/c, and whose daughters should always be considered primary. The mean proper lifetime of the parent is used to judge whether or not the daughter is treated as primary. A decay product is considered primary if its parent has a mean proper lifetime τ satisfying ~~$c\tau <$~~ $\tau < \tau_{\max}$, where $c\tau_{\max} =$ 10 fm ~~. Changing $c\tau$~~ for this analysis. Changing $\tau_{\max}$ only moderately affects the λ_{ij} parameters, and the effect is included in the estimation of the systematic uncertainties. In order for a pair to be considered primary, both particles in the pair must be considered primary. If either parent has $\tau > \tau_{\max}$, the daughter pair contributes to the "Other" category when calculating ~~λ~~ λ_{ij} parameters. For this mixture of pair systems, all with different two-particle interactions and single-particle source distributions, the net correlation effect is ~~assumed~~ taken to average to unity.

Residual contributions from Σ^0, Ξ^0, Ξ^- are accounted for in the fit. The λ_{ij} values used can be found in Table 4, which also ~~included~~ includes values for "Other" and "Fakes". The "Other" category contains pairs which are not considered primary, and which do not originate from the residual contributors accounted for in the fit. The "Fakes" category represents pairs that are mistakenly identified as ΛK. ~~To estimate the~~ The corresponding λ_{Fakes} ~~value, the number of fake pairs is assumed to be equal to the total number of simulated pairs multiplied by $(1 - PP_{\Lambda\mathrm{K}})/PP_{\Lambda\mathrm{K}}$~~ is calculated as $\lambda_{\mathrm{Fakes}} = 1 - PP_{\Lambda\mathrm{K}}$, where $PP_{\Lambda\mathrm{K}}$ is the ΛK pair purity, estimated as the product of the two single-particle purities ($PP_{\Lambda\mathrm{K}} = P_\Lambda P_\mathrm{K}$). ~~More simply, this amounts to $\lambda_{\mathrm{Fakes}} = 1.0 - PP_{\Lambda\mathrm{K}}$.~~ The correlations in both of these categories ("Other" and "Fakes") are assumed to average to unity, and pairs in these categories therefore only contribute by attenuating the signal.

~~Weight parameters (λ_{ij}) for the individual components of the correlation functions~~

~~**Source λ value Source λ value Source λ value Source λ value** Primary 0.527 Primary 0.526 Primary 0.526 Primary 0.527 Σ^0K$^+$ 0.111 $\overline{\Sigma}^0$K$^-$ 0.110 Σ^0K$^-$ 0.110 $\overline{\Sigma}^0$K$^+$ 0.111 Ξ^0K$^+$ 0.039 $\overline{\Xi}^0$K$^-$ 0.035 Ξ^0K$^-$ 0.038 $\overline{\Xi}^0$K$^+$ 0.036 Ξ^-K$^+$ 0.050 $\overline{\Xi}^+$K$^-$ 0.046 Ξ^-K$^-$ 0.050 $\overline{\Xi}^+$K$^+$ 0.046 Other 0.226 Other 0.235 Other 0.228 Other 0.233 Fakes 0.048 Fakes 0.048 Fakes 0.048 Fakes 0.048~~

~~**Source λ value Source** Primary 0.543 Primary Σ^0K$^0_\mathrm{S}$ 0.120 $\overline{\Sigma}^0$K$^0_\mathrm{S}$ Ξ^0K$^0_\mathrm{S}$ 0.042 $\overline{\Xi}^0$K$^0_\mathrm{S}$ Ξ^-K$^0_\mathrm{S}$ 0.054 $\overline{\Xi}^+$K$^0_\mathrm{S}$ Other 0.194 Other Fakes 0.048 Fakes~~

3.4 Momentum resolution corrections

Finite track momentum resolution causes the reconstructed ~~momentum of a particle to smear around the true value. This, of course, also holds true for particles. The effect is propagated up to the pairs of interest, which causes the reconstructed~~ relative momentum (k^*_Rec) of a pair to differ from the true ~~momentum~~ value (k^*_True). ~~The effects of finite momentum resolution are~~ This is accounted for through the use of a response matrix generated with HIJING simulations. With this approach, the resolution correction is applied on-the-fly during the fitting process by propagating the theoretical (fit) correlation function through the response matrix, according to

$$C_{\mathrm{fit}}(k^*_\mathrm{Rec}) = \frac{\sum\limits_{k^*_\mathrm{True}} M_{k^*_\mathrm{Rec}, k^*_\mathrm{True}} C(k^*_\mathrm{True})}{\sum\limits_{k^*_\mathrm{True}} M_{k^*_\mathrm{Rec}, k^*_\mathrm{True}}}, \tag{10}$$

where $M_{k^*_\mathrm{Rec}, k^*_\mathrm{True}}$ is the response matrix, ~~$C_{\mathrm{fit}}(k^*_\mathrm{True})$ is the fit~~ $C(k^*_\mathrm{True})$ is the correlation as a function of k^*_True, and the denominator normalizes the result. ~~Equation 10 describes that, for a given , the observed value~~

Table 4: Weight parameters (λ_{ij}) for the individual components of the ΛK correlation functions

ΛK$^+$		$\overline{\Lambda}$K$^-$		ΛK$^-$		$\overline{\Lambda}$K$^+$	
Source	λ value	Source	λ value	Source	λ value	Source	λ value
Primary	~~0.527~~ 0.509	Primary	~~0.526~~ 0.509	Primary	~~0.526~~ 0.509	Primary	~~0.527~~ 0.510
Σ^0K$^+$	~~0.111~~ 0.108	$\overline{\Sigma}^0$K$^-$	~~0.110~~ 0.107	Σ^0K$^-$	~~0.110~~ 0.107	$\overline{\Sigma}^0$K$^+$	~~0.111~~ 0.108
Ξ^0K$^+$	~~0.039~~ 0.037	$\overline{\Xi}^0$K$^-$	~~0.035~~ 0.034	Ξ^0K$^-$	~~0.038~~ 0.037	$\overline{\Xi}^0$K$^+$	~~0.036~~ 0.035
Ξ^-K$^+$	~~0.050~~ 0.048	$\overline{\Xi}^+$K$^-$	~~0.046~~ 0.044	Ξ^-K$^-$	~~0.050~~ 0.048	$\overline{\Xi}^+$K$^+$	~~0.046~~ 0.045
Other	~~0.226~~ 0.218	Other	~~0.235~~ 0.228	Other	~~0.228~~ 0.221	Other	~~0.233~~ 0.225
Fakes	~~0.048~~ 0.079	Fakes	~~0.048~~ 0.079	Fakes	~~0.048~~ 0.079	Fakes	~~0.048~~ 0.079

ΛK$_S^0$		$\overline{\Lambda}$K$_S^0$	
Source	λ value	Source	λ value
Primary	~~0.543~~ 0.531	Primary	0.532
Σ^0K$_S^0$	~~0.120~~ 0.118	$\overline{\Sigma}^0$K$_S^0$	0.118
Ξ^0K$_S^0$	~~0.042~~ 0.041	$\overline{\Xi}^0$K$_S^0$	0.038
Ξ^-K$_S^0$	~~0.054~~ 0.053	$\overline{\Xi}^+$K$_S^0$	0.049
Other	~~0.194~~ 0.189	Other	0.195
Fakes	~~0.048~~ 0.069	Fakes	0.069

~~of $C(k^*_{\mathrm{Rec}})$ is a weighted average of all $C(k^*_{\mathrm{True}})$ values, where the weights are the normalized number of counts in the $[k^*_{\mathrm{Rec}}, k^*_{\mathrm{True}}]$ bin.~~

3.5 Non-femtoscopic background

A significant non-femtoscopic background is observed in all of the studied ΛK correlations, which increases with decreasing centrality, is the same amongst all ΛK$^\pm$ pairs, and is more pronounced in the ΛK$_S^0$ system (the difference in ΛK$^\pm$ and ΛK$_S^0$ backgrounds is due mainly to a difference in kinematic selection criteria). The background is primarily due to particle collimation associated with elliptic flow, and results from mixing events with unlike event planes [33]. The effect produces the observed suppression at intermediate k^*, and should also lead to an enhancement at low k^*. ~~The behavior~~ To best describe the experimental data, an understanding of the non-femtoscopic background is needed in the low k^* femtoscopic signal region, but an isolated view of it is only possible outside of such a region.

The THERMINATOR 2 simulation has been shown to reproduce the background features in a ~~ππK~~ πK analysis [33]. ~~The simulation does not include any final-state effects, but they can be introduced by weighting the numerator pairs with the modulus squared of the appropriate two-particle wave-function when building the signal distributions. For the present purpose, only the behavior of the non-femtoscopic background is desired, and unit weights are used.~~ Figure 2 shows the THERMINATOR 2 simulation together with experimental data. The figure also shows a ~~6th-order~~ sixth-order polynomial fit to the simulation, as well as the fit polynomial scaled to match the data.

~~The~~ Clearly, the THERMINATOR 2 simulation offers a good description of the non-femtoscopic backgrounds in the ΛK systems, and can be used in a quantitative fashion to help fit the data. More specifically, the non-femtoscopic backgrounds are modeled by ~~6th-order~~ sixth-order polynomial fits to THERMINATOR 2 simulation,

$$F_{\underline{\mathrm{THERM.\,Bgd}}\,\mathrm{THERM\,Bgd}}(k^*) = ak^{*6} + bk^{*5} + ck^{*4} + dk^{*3} + ek^{*2} + fk^* + g, \qquad (11)$$

where the linear term coefficient is fixed to zero ($f = 0$), and one polynomial is fit for each centrality

365 class and ΛK charge combination. ~~The~~

366 Before fitting the signal region of the experimental data, the coefficients of each polynomial are ~~set before~~

367 ~~application with the experimental data by fitting~~ fixed by fits to the THERMINATOR 2 ~~simulation~~background,

368 shown in Fig. 2. The extracted polynomial is adjusted to best describe the experimental data by intro-

369 ducing a scale factor and a vertical shift,

$$F_{\underline{Bgd}\text{Bgd}}(k^*) = \alpha \cdot F_{\underline{THERM.\,Bgd}\text{THERM Bgd}}(k^*) + \beta, \tag{12}$$

370 where α and β are determined by fitting to the data in the region $0.32 < k^* < 0.80$ GeV/c; ~~during the~~

371 ~~fit of the~~all of the background parameters in Eq. (11) and Eq. (12) are fixed before fitting the low-k^*

372 signal region ~~, the background is fixed~~of the experimental correlation functions. In all cases, the non-

373 femtoscopic background correction was applied as a ~~scale factor~~ multiplicative factor to the correlation

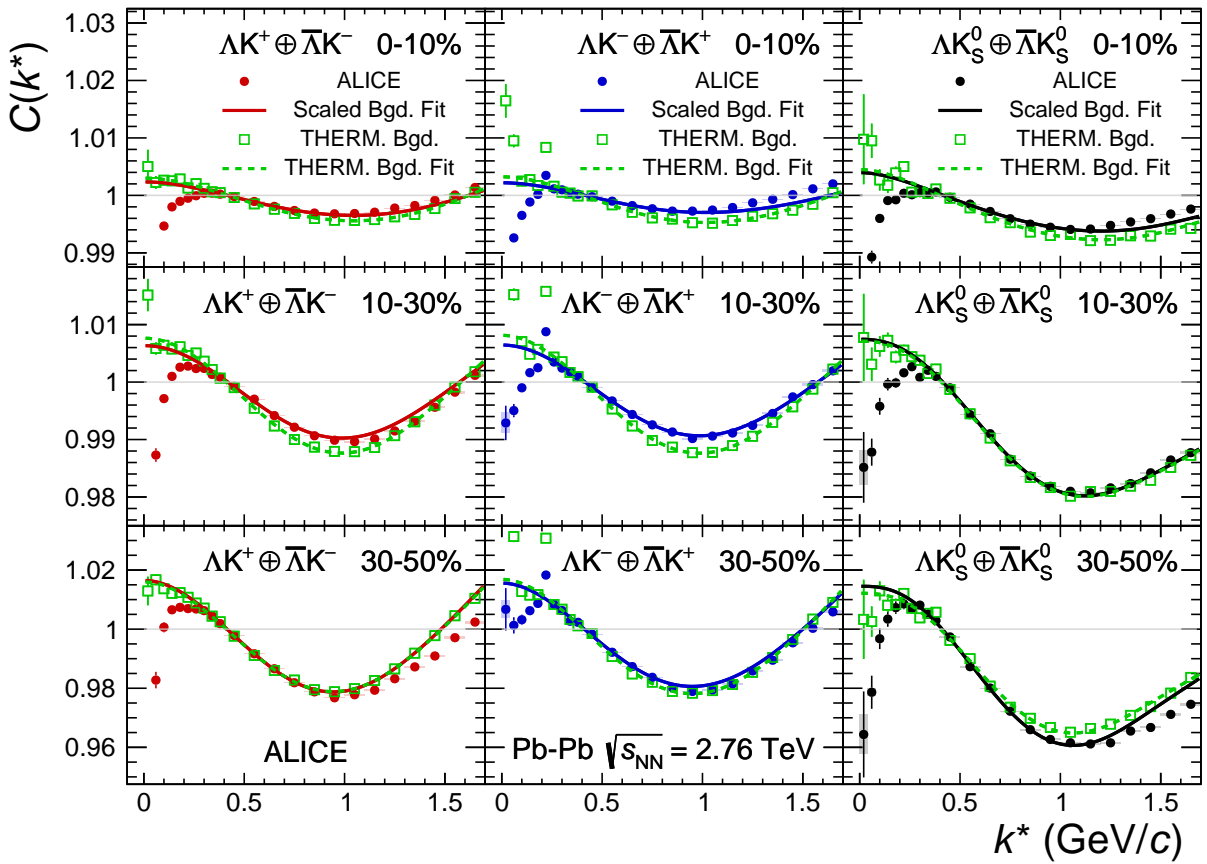374 function during the fitting process.

Figure 2: (Color online) THERMINATOR 2 simulation (open squares) together with experimental data (closed circles). Results are shown for ΛK$^+$ (left), ΛK$^-$ (middle), and ΛK$_S^0$ (right). ~~A 6th-order~~ Rows differentiate the different centrality intervals (0–10% in the top, 10–30% in the middle, and 30–50% in the bottom). A sixth-order polynomial fit to the simulation is shown as a dashed curve. This polynomial is scaled to match the experimental data ~~. The polynomial fit with scale factor applied~~ and is drawn as a solid curve.

375 An alternative approach to treating the non-femtoscopic background is to instead attempt to eliminate

376 it. The background ~~may~~ can be effectively reduced by forming the reference distribution ($B(k^*)$) with

377 the "Stavinskiy method"~~. With the Stavinskiy~~ [34, 35] (see Appendix A for details). With this method,

378 mixed-event pairs are not used for the reference distribution; instead, same-event pseudo-pairs, formed

379 by rotating one particle in a real pair by 180° in the transverse plane, are used. This rotation rids the pairs

380 of any femtoscopic correlation, while maintaining correlations due to elliptic flow (and other suitably

13

symmetric contributors). The flattening effect of the method on the ΛK^+ correlation functions can be seen in the ~~appendix, in Fig. A.1~~Appendix A.

3.6 Summarized correlation function construction

The parameters included in the generation of a model correlation function are: λ_{Fit}, R, f_0 ($\Re f_0$ and $\Im f_0$ separately), d_0, and normalization $\mathcal{N}$. For the fit, a given pair and its conjugate (e.g., ΛK^+ and $\overline{\Lambda} K^-$) share scattering parameters ($\Re f_0$, $\Im f_0$, d_0), and the three distinct analyses (ΛK^+, ΛK^-, and ΛK_S^0) are assumed to have ~~scattering parameters unique~~ unique scattering parameters which are allowed to differ from each other. The pair emission source for a given centrality class is assumed similar among all analyses; therefore, for each centrality, all ΛK analyses share a common radius parameter~~. For~~, R. Furthermore, for each centrality class, a single λ_{Fit} parameter (see Eq. ~~6~~(6)) is shared amongst all. ~~Finally, each~~Each fit correlation function has a unique normalization parameter, $\mathcal{N}$.

The experimental correlation functions were constructed separately for the two different field polarities applied by the ALICE L3 solenoid magnet during the data acquisition. These are kept separate during the fitting process, and are combined using a weighted average when plotting, where the weight is the number of numerator pairs in the normalization range. All experimental correlation functions are normalized in the range $0.32 < k^* < 0.40$ GeV/c, and fit in the range $0.0 < k^* < 0.30$ GeV/c. For the ΛK^- analysis, the region $0.19 < k^* < 0.23$ GeV/c was excluded from the fit to exclude the bump caused by the Ω^- resonance. ~~For each pair system, contributions from three residual contributors are accounted for, as discussed in Sec. 3.3, and whose individual λ values are listed in Table 4. Effects of finite track momentum resolution are also accounted for, as outlined in Sec. 3.4. The non-femtoscopic backgrounds are modeled using the THERMINATOR 2 simulation, as described in Sec. 3.5~~decay. A log-likelihood fit function is used as the statistic quantifying the quality of the fit to the experimental data [1].

~~To summarize, the~~The complete fit function is constructed as follows. The uncorrected, primary, fit correlation function, $C_{\Lambda K}(k^*_{\Lambda K,\mathrm{True}})$, is constructed using Eq. ~~5. The~~(5). Contributions from three parent systems which contribute via residual correlations are accounted for, as discussed in Sec. 3.3. The model correlation functions describing ~~the parent systems~~which contribute residually~~these parent systems, $C_{ij}(k^*_{ij,\mathrm{True}})$, are obtained using Eq. ~~5~~(5) for Coulomb-neutral pairs or experimental data for $\Xi^- K^{\pm}$ contributions. The residual contributions are then found by running each parent correlation function through the appropriate transform matrix, via Eq. ~~8. The~~(8). The model primary and residual ~~correlations~~contributions are combined, via Eq. ~~6 with~~(6) with the λ_{ij} values listed in Tab. 4, to form ~~C'_{Fit}~~$C'_{\mathrm{Fit}}(k^*_{\mathrm{True}})$. Corrections are applied to account for finite track momentum resolution effects using Eq. ~~10~~(10), to obtain $C'_{\mathrm{Fit}}(k^*_{\mathrm{Rec}})$. Finally, the non-femtoscopic background correction, $F_{\mathrm{Bgd}}(k^*_{\mathrm{Rec}})$, is applied as described in Sec. 3.5, and the final fit function is obtained,

$$C_{\mathrm{Fit}}(k^*_{\mathrm{Rec}}) = \mathcal{N} \cdot F_{\mathrm{Bgd}}(k^*_{\mathrm{Rec}}) \cdot C'_{\mathrm{Fit}}(k^*_{\mathrm{Rec}}), \tag{13}$$

where $\mathcal{N}$ is a normalization parameter. ~~$C'_{\mathrm{Fit}}(k^*_{\mathrm{Rec}})$ includes all components of the correlation function weighted by the appropriate λ_{ij} (see Sec. 3.3) parameters and has been corrected for momentum resolution effects (see Sec. 3.4)~~This model correlation function is then fit to the experimental correlation function.

3.7 Systematic uncertainties

To estimate the systematic uncertainties in the analysis, the selection criteria were varied, and experimental correlation functions and fit results were obtained for each variation. ~~The selection criteria included in the systematic study, as well as the values used in the variations, are shown in Tab. ??. Note, in each case, the central value corresponds to that used in the analysis.~~To quantify the systematic uncertainties on the data ~~, the~~points, the experimental correlation functions from each variation of the selection criteria were ~~averaged, and~~combined, giving a distribution of values for each k^*. From these distributions, the

standard deviations were calculated ~~for each data point. The~~ and assigned as the systematic uncertainties of the ~~correlation functions were set to these calculated standard deviations~~ corresponding data points.

A similar process was followed for estimating the systematic uncertainties of the extracted fit parameters. Namely, the extracted fit parameters from each variation were averaged, and the resulting standard deviations taken as the systematic uncertainties. Additionally, a systematic analysis was done on the fit method through varying the k^* fit range, varying the modeling of the non-femtoscopic background, as well as varying τ_{max} in the treatment of residual correlations. The choice of k^* fit range was varied by $\pm 25\%$. In addition to modeling with a polynomial fit to the THERMINATOR 2 simulation, the backgrounds of all of the systems were modeled by fitting to the data with a linear, quadratic, and Gaussian form. Finally, τ_{max} was varied from the default value of $\tau_{\mathrm{max}} = 10$ fm/c down to $\tau_{\mathrm{max}} = 6$ fm/c and up to $\tau_{\mathrm{max}} = 15$ fm/c. The resulting uncertainties in the extracted parameter sets were combined with the uncertainties arising from the variations of the selection criteria.

~~Selection parameter variation for the study of systematic uncertainties in the analysis. In the table, the shorthand used is as follows: PA = pointing angle; PV = primary vertex; DCA = distance of closest approach; $\overline{\Delta \mathbf{r}}$ = average separation DCA to PV < 0.4, 0.5, 0.6cm DCA to PV < 0.2, 0.3, 0.4cm DCA Daughters < 0.3, 0.4, 0.5cm DCA Daughters < 0.2, 0.3, 0.4cm $\cos(\theta_{\mathrm{PA}})$ to PV > 0.9992, 0.9993, 0.9994 $\cos(\theta_{\mathrm{PA}})$ to PV > 0.9992, 0.9993, 0.9994 DCA to PV of p$(\overline{\mathrm{p}})$ Daughter of > 0.05, 0.1, 0.2cm DCA to PV of $\pi^-(\pi^+)$ Daughter of > 0.2, 0.3, 0.4cm DCA to PV of π^+ Daughter of > 0.2, 0.3, 0.4cm DCA to PV of π^- Daughter of > 0.2, 0.3, 0.4cm $\overline{\Delta \mathbf{r}}$ of Like-Charge Daughters > 5, 6, 7cm~~

~~DCA to PV < 0.4, 0.5, 0.6cm DCA Daughters < 0.3, 0.4, 0.5cm $\cos(\theta_{\mathrm{PA}})$ to PV > 0.9992, 0.9993, 0.9994 DCA to PV of p$(\overline{\mathrm{p}})$ Daughter of > 0.05, 0.1, 0.2cm DCA to PV of $\pi^-(\pi^+)$ Daughter of > 0.2, 0.3, 0.4cm $\overline{\Delta \mathbf{r}}$ of Daughter with Same Charge as > 7, 8, 9cm DCA to PV in Transverse Plane of < 1.92, 2.4, 2.88cm DCA to PV in Longitudinal Direction of < 2.4, 3.0, 3.6cm~~

The systematic uncertainties of the extracted parameters sets are due primarily to the fit method variations, i.e., the selection criteria do not contribute significantly.

4 Results

Figure 3 shows the ΛK data with fits for all studied centrality percentile intervals (0–10%, 10–30%, and 30–50%). All six ΛK systems (ΛK$^+$, $\overline{\Lambda}$K$^-$, ΛK$^-$, $\overline{\Lambda}$K$^+$, ΛK$_{\mathrm{S}}^0$, $\overline{\Lambda}$K$_{\mathrm{S}}^0$) are fit simultaneously across all centralities, with a single radius and normalization λ_{Fit} parameter for each centrality interval. ~~Scattering parameters ($\Re f_0$, $\Im f_0$, d_0) are shared between pair-conjugate systems, but assumed unique among the different charge combinations (i.e., a parameter set describing the & system, a second set describing the & system, and a third for the & system). Each correlation function receives a unique normalization parameter. The fits are corrected for finite momentum resolution effects, non-femtoscopic backgrounds, and residual correlations resulting from the feed-down from resonances.~~ The figure shows the primary (ΛK) contribution to the fit (i.e., $1 + \lambda'_{\Lambda \mathrm{K}} C_{\Lambda \mathrm{K}}(k^*_{\Lambda \mathrm{K}})$ in Eq. ~~6~~ (6)), the fit to the non-femtoscopic background, and the final fit, with all residual contributions included and after all corrections have been applied. The extraction of the primary ΛK component is the purpose of this study. The figure demonstrates that the final fit function is similar to the primary ΛK component, with the largest differences between the two observed in the 30–50% centrality interval due mainly to the large contribution of the non-femtoscopic background.

Figure 4 (left) summarizes the extracted ΛK scattering parameters, and includes theoretical predictions made using chiral perturbation theory [11, 12]. For all ΛK systems, positive imaginary parts of the scattering lengths, $\Im(f_0)$, are extracted from the experimental data. This is expected, as $\Im(f_0)$ describes the inelastic scattering channels. More interestingly, the results show that the ΛK$^+$ and ΛK$^-$ systems differ in the sign of the real part, $\Re(f_0)$, of their scattering lengths, with a negative value for ΛK$^+$ and
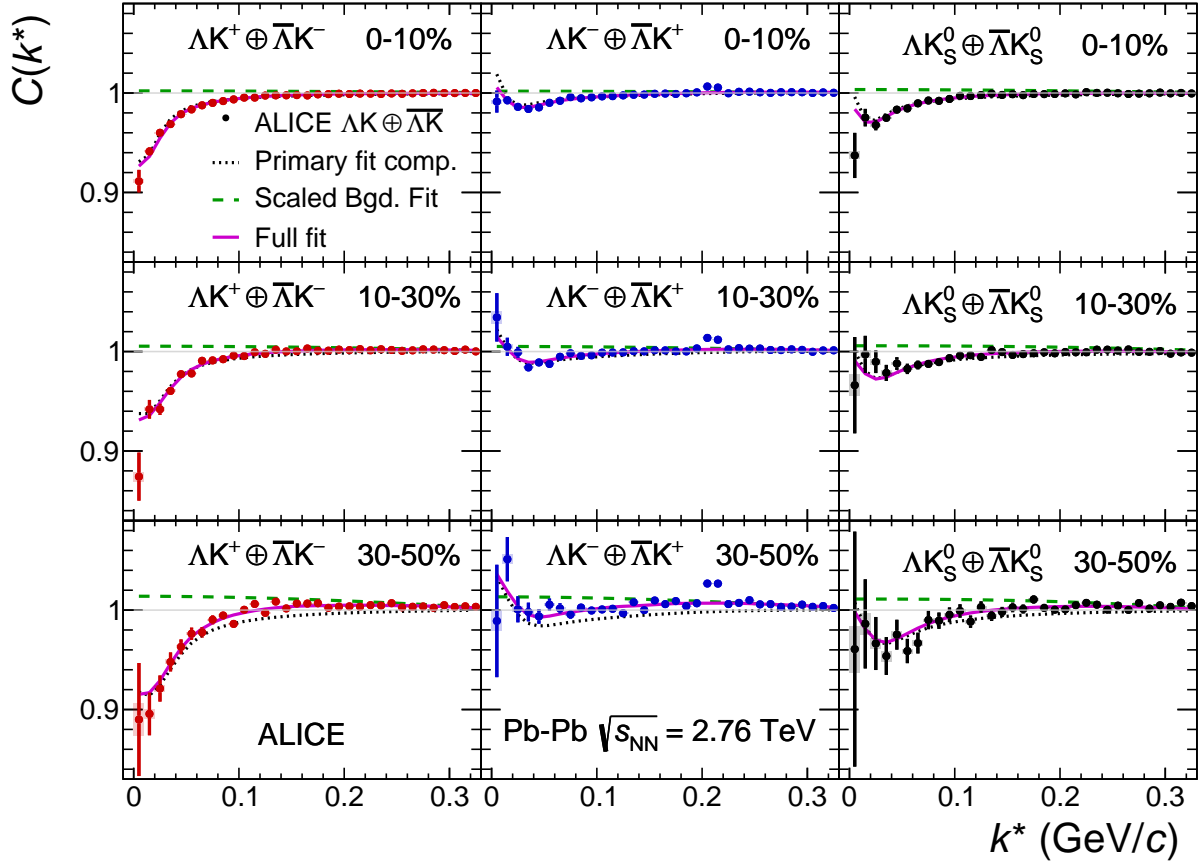
Figure 3: (Color online) Fit results for the ΛK data, with pair and conjugate combined. The $\Lambda K^+ \oplus \overline{\Lambda} K^-$ data are shown in the left column, the $\Lambda K^- \oplus \overline{\Lambda} K^+$ in the middle, and the $\Lambda K_S^0 \oplus \overline{\Lambda} K_S^0$ in the right. Rows differentiate the different centrality intervals (0–10% in the top, 10–30% in the middle, and 30–50% in the bottom). Lines represent statistical uncertainties, while boxes represent systematic uncertainties. The dotted curve shows the primary (ΛK) contribution to the fit, the dashed curve shows the fit to the non-femtoscopic background, and the solid curve shows the final fit.

469 positive value for ΛK^-. The $\Re f_0$ extracted for the ΛK_S^0 system is positive, and within uncertainties of
470 that of ~~the~~ ΛK^-. The real part of the scattering length describes the effect of the strong interaction,
471 ~~making the difference in these systems quite intriguing. As is the usual convention in femtoscopy,~~ : a
472 positive $\Re(f_0)$ signifies that the ~~effect of the~~ interaction is attractive, while a negative $\Re(f_0)$ signifies
473 a repulsive interaction, as is the usual convention in femtoscopy. Therefore, the femtoscopic signals
474 from this analysis demonstrate that the strong interaction acts repulsively in the ΛK^+ system, and acts
475 attractively in the ΛK^- and ΛK_S^0 systems. Finally, the results indicate that the effective range of the
476 interaction, d_0, is positive in the ΛK^+ system and negative in the ΛK^- and ΛK_S^0 systems.

477 In Fig. 4 (left), the predictions of [11] do not distinguish the KΛ and $\overline{K}\Lambda$ interactions and results are
478 shown for two different parameter sets, whereas [12] offers unique KΛ and $\overline{K}\Lambda$ scattering parameters
479 for a single parameter set. In all cases, the predicted scattering parameters have both positive real and
480 imaginary components, which is ~~clearly~~ inconsistent with the ΛK^+ system. Past studies of kaon-proton
481 scattering found the K^-–~~p~~ p interaction to be attractive, and that of the K^+–~~p~~ p to be repulsive [13–15].
482 With respect to the kaons, this is similar to the current finding of an attractive ~~–~~ ΛK^- interaction and a
483 repulsive ~~–~~ ΛK^+ interaction. This difference could ~~be due to an effect arising~~ arise from different quark–
484 antiquark interactions between the pairs ($s\bar{s}$ in ΛK^+, $u\bar{u}$ in ΛK^-). A related explanation could be that
485 the effect is due to the different net strangeness for each system. The quark content of the Λ ($\overline{\Lambda}$) is uds
486 ($\overline{uds}$), that of the K^+ (K^-) is $u\bar{s}$ ($\overline{u}s$), and the K_S^0 is a mixture of the neutral K^0 and $\overline{K^0}$ states with quark
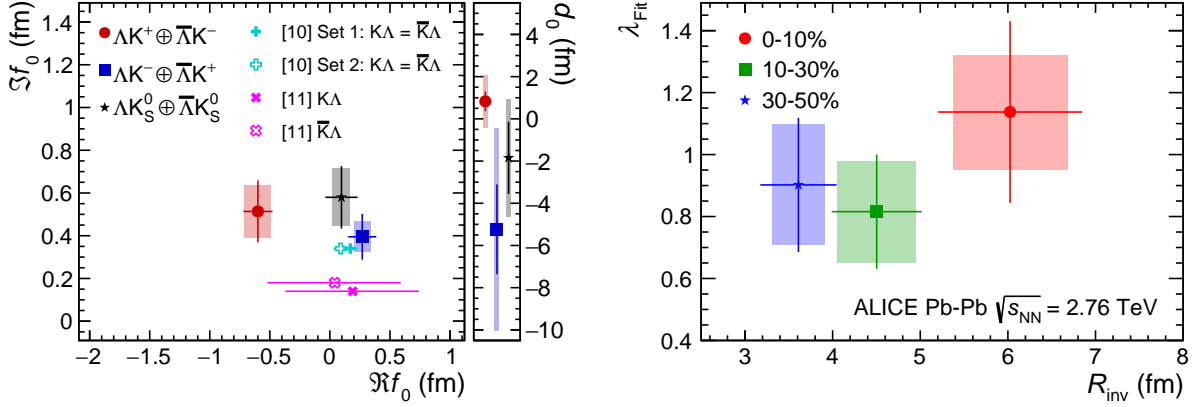
Figure 4: (Color online) Extracted fit parameters for all of the ΛK systems. (Left) The scattering parameters, $\Im f_0$ and $\Re f_0$, together with d_0 to the right, for the ΛK^+ (circles), ΛK^- (squares) and ΛK_S^0 (stars) systems. (Right) The λ_{Fit} and radius parameters for the 0–10% (circles), 10–30% (squares), and 30–50% (stars) centrality intervals. In the fit, all ΛK systems share common radii. The cross [11] and X [12] points show theoretical predictions made using chiral perturbation theory.

487 content $\frac{1}{\sqrt{2}} \left[d\bar{s} + \bar{d}s \right]$. It is interesting to note the presence of a $s\bar{s}$ pair in the ΛK^+ system contrasted with

488 a $u\bar{u}$ pair in the ΛK^- system. Additionally, although the K_S^0 is ~~a type~~ an average of K^+ and K^- in some

489 respects (e.g., electrically), it contains (anti)down quarks, whereas the $K^\pm$ contain (anti)up quarks.
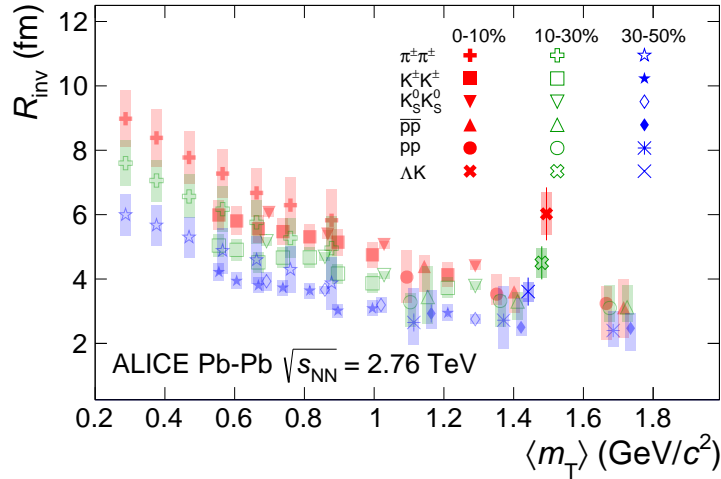
Figure 5: (Color online) Extracted fit R_{inv} parameters as a function of pair transverse mass (m_T) for several centralities. Results from the ΛK analysis are presented together with ALICE published data [36] for various other pair systems.

490 Figure 4 (right) presents the λ_{Fit} and radius parameters for all three studied centrality percentile ranges.

491 The λ_{Fit} parameters are expected to be close to unity. A comparison of the extracted radii from this study

492 to those of other systems measured by ALICE [36] is shown in Fig. 5. The figure shows ~~extracted~~ R_{inv} as

493 a function of m_T for several centrality ranges and for several different pair systems. The m_T value used

494 for the present ΛK results was taken as the average of the three systems. For non-identical particle pairs,

495 to be more directly analogous to the single particle m_T, the definition of the pair transverse mass used in

496 this study is

$$m_{T,\text{pair}}^2 = \left(\frac{m_{\text{inv}}}{2} \right)^2 + \left(\frac{1}{2} | \boldsymbol{p}_{T,1} + \boldsymbol{p}_{T,2} | \right)^2 = (K^0)^2 - (K^3)^2, \quad \text{where } K^\mu \equiv \frac{1}{2} \left(p_1^\mu + p_2^\mu \right). \quad (14)$$

497 The radii are observed to increase for more central events, as expected from a simple geometric picture

of the collisions. ~~For~~ Femtoscopy probes the distribution of relative positions of outgoing particles whose velocities have a specific magnitude and direction [1], referred to as "regions of homogeneity" [9]. Consequently, for each pair system, the radii decrease with increasing m_T, as expected in the presence of collective radial flow [9]. It was found that [37], even in the presence of ~~good~~ global m_T-scaling for the three-dimensional radii in the Longitudinally Co-Moving System (LCMS), a particle species dependence will exist for the R_{inv} measured in the PRF, due to trivial kinematic reasons. These kinematic effects, resulting from the transformation from LCMS to PRF, cause smaller masses to exhibit larger R_{inv} [36] (explaining, for instance, ~~how~~ why the pion radii are systematically higher than kaon radii at the same approximate m_T).

It is clear from the results in Fig. 5 that the ΛK systems do not conform to the approximate m_T-scaling of the identical particle pair source sizes. ~~The~~ There are two important consequences of the hydrodynamic nature of the system to consider when interpreting non-identical femtoscopic results. First, the hydrodynamic response of the medium produces the approximate m_T-scaling with respect to the single-particle sources~~, not the pair sources. Furthermore, the hydrodynamic response not only~~. Second, this response confines higher-m_T particles to smaller homogeneity regions ~~, it also~~ and pushes their average emission points further in the "out" direction [7] ~~,~~ in a coordinate system chosen according to the out-side-long prescription (where the "long" axis is parallel to the beam, "out" is parallel to the total transverse momentum of the pair, and "side" is orthogonal to both). For identical particle studies, in which the pair source is comprised of two identical single particle sources commonly affected by the space-time shift, the femtoscopic radii naturally follow the m_T-scaling trend. However, for the case of non-identical particles, the pair emission source is a superposition of two unique single-particle sources, which are affected differently by the hydrodynamic response of the system. Therefore, the Λ and K sources differ both in size and space–time location, leading to an "emission asymmetry", with the Λ source both smaller in size and further out in the fireball than that of the kaons.

A separation of the single-particle sources in the "out" direction is expected for ΛK pairs at mid-rapidity in Pb–Pb collisions, as described above, and the experimental data support such an emission asymmetry. In addition to the "size" of the emitting region (more precisely, the second moments of the emission functions) accessible with identical particle studies, non-identical particle correlations are sensitive to the relative emission shifts, i.e., the first moments of the emission function [10]. The spherical harmonic decomposition of the correlation function offers an elegant method for extracting information about the emission asymmetries [38–40]. With this method, one can draw a wealth of information from just a few components of the decomposition. Particularly, the $l = 0$, $m = 0$ component, C_{00}, ~~is similar to the one-dimensional correlation functions typically studied~~ quantifies the angle-integrated strength of the correlation function, and probes the overall size of the source. Of interest here, the real part of the $l = 1$, $m = 1$ component, $\Re C_{11}$, probes the asymmetry of the system in the "out" direction; a non-zero value reveals the asymmetry. Figure 6 shows the C_{00} and $\Re C_{11}$ components from the spherical decomposition of the ΛK^+ data in the 0–10% centrality interval. The $\Re C_{11}$ component shows a clear deviation from zero, and the negative value signifies that the Λ particles are, on average, emitted further out and/or earlier than the K mesons. This conclusion is supported by the results obtained from the THERMINATOR 2 model, shown in Fig. C.1. Furthermore, this emission asymmetry effect can inflate the radii extracted with the one-dimensional Lednický model, which assumes a spherically symmetric source with no offsets (i.e., $R_{out} = R_{side} = R_{long}$ and $\mu_{out} = \mu_{side} = \mu_{long} = 0$). This effect is demonstrated in Appendix C using the THERMINATOR 2 simulation. In Fig. 5, the largest violation of the m_T-scaling for the ΛK system is observed for the 0–10% centrality interval, in which one expects the largest emission asymmetry.

5   Summary

Results from a femtoscopic analysis of ΛK correlations in Pb–Pb collisions at $\sqrt{s_{NN}}$ = 2.76 TeV measured by the ALICE experiment at the LHC have been presented, and are summarized in Table 5. The
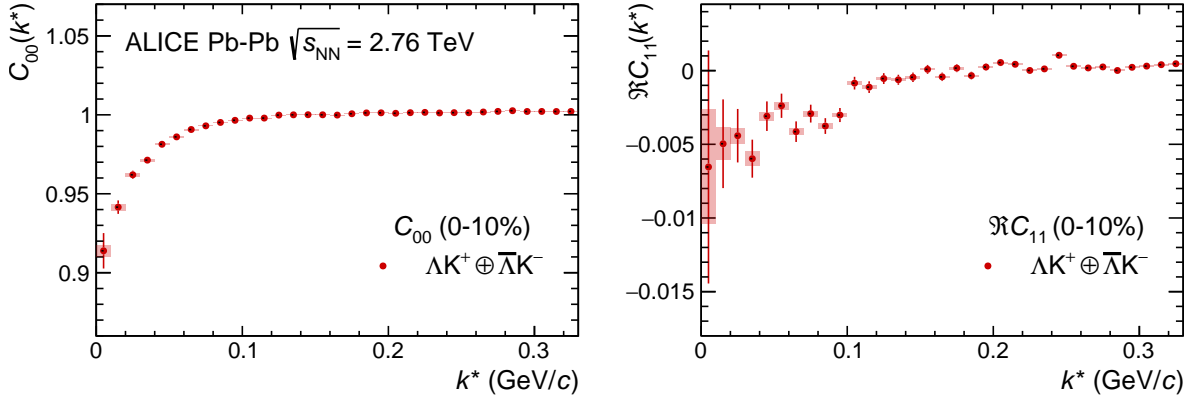
Figure 6: (Color online) Spherical harmonics components C_{00} (left) and $\Re C_{11}$ (right) of the ΛK^+ correlation function for the 0–10% centrality interval. The C_{00} component is similar to the one-dimensional correlation functions typically studied, and probes the overall size of the source. The $\Re C_{11}$ component probes the asymmetry in the system; a non-zero value reveals the asymmetry.

Table 5: Extracted fit parameters. The uncertainties marked as "stat." are those returned by MINUIT, and those marked as "syst." result from the systematic analysis.

Centrality	λ_{Fit}	R_{inv}
0–10%	1.14 ± 0.29 (stat.) ± 0.18 (syst.)	6.02 ± 0.82 (stat.) ± 0.65 (syst.)
10–30%	0.82 ± 0.18 (stat.) ± 0.16 (syst.)	4.50 ± 0.51 (stat.) ± 0.45 (syst.)
30–50%	0.90 ± 0.22 (stat.) ± 0.19 (syst.)	3.61 ± 0.44 (stat.) ± 0.30 (syst.)

System	$\Re f_0$	$\Im f_0$	d_0
$\Lambda K^+ \oplus \overline{\Lambda} K^-$	-0.60 ± 0.12 (stat.) ± 0.11 (syst.)	0.51 ± 0.15 (stat.) ± 0.12 (syst.)	0.83 ± 0.47 (stat.) ± 1.23 (syst.)
$\Lambda K^- \oplus \overline{\Lambda} K^+$	0.27 ± 0.12 (stat.) ± 0.07 (syst.)	0.40 ± 0.11 (stat.) ± 0.07 (syst.)	-5.23 ± 2.13 (stat.) ± 4.80 (syst.)
$\Lambda K_S^0 \oplus \overline{\Lambda} K_S^0$	0.10 ± 0.13 (stat.) ± 0.07 (syst.)	0.58 ± 0.15 (stat.) ± 0.13 (syst.)	-1.85 ± 1.71 (stat.) ± 2.77 (syst.)

545 femtoscopic radii, λ parameters, and scattering parameters were extracted from one-dimensional cor-
546 relation functions in terms of the invariant momentum difference. The scattering parameters of ΛK
547 pairs in all three charge combinations (ΛK^+, ΛK^-, and ΛK_S^0) ~~have been~~ were measured for the first
548 time. The non-femtoscopic backgrounds observed in the experimental data were described quantitatively
549 with the THERMINATOR 2 event generator, and were found to result almost entirely from collective
550 effects. Striking differences are observed in the ΛK^+, ΛK^-, and ΛK_S^0 correlation functions, which are
551 reflected in the unique set of scattering parameters extracted for each. ~~The extracted~~ These scattering
552 parameters indicate that the strong force is repulsive in the ΛK^+ interaction and attractive in the ΛK^-
553 and ΛK_S^0 interactions. This effect could be due to different quark–antiquark interactions between the
554 pairs, or from different net strangeness ~~for~~ present in each system. The ~~non-femtoscopic background is~~
555 ~~found to result almost entirely from collective effects, and is described quantitatively with unprecedented~~
556 ~~precision with the THERMINATOR 2 event generator. Finally,~~ extracted source radii describing the ΛK
557 systems ~~exhibit source radii~~ are larger than expected from ~~extrapolation from~~ naive extrapolation of iden-
558 tical particle femtoscopic studies. This effect is interpreted as resulting from the separation in space–time
559 of the single-particle Λ and K source distributions (i.e., the emission asymmetry of the source), which is
560 confirmed by the spherical harmonics decomposition of the correlation functions.

Acknowledgements

References

[1] M. A. Lisa, S. Pratt, R. Soltz, and U. Wiedemann, "Femtoscopy in relativistic heavy ion collisions", *Ann. Rev. Nucl. Part. Sci.* **55** (2005) , `arXiv:nucl-ex/0505014 [nucl-ex]`.

[2] G. I. Kopylov and M. I. Podgoretsky, "Correlations of identical particles emitted by highly excited nuclei", *Sov. J. Nucl. Phys.* **15** (1972) . [Yad. Fiz.15,392(1972)].

[3] M. A. Lisa and S. Pratt, "Femtoscopically Probing the Freeze-out Configuration in Heavy Ion Collisions", in *Relativistic Heavy Ion Physics*, R. Stock, ed. 2010. `arXiv:0811.1352 [nucl-ex]`.

[4] R. Lednický, V. L. Lyuboshitz, B. Erazmus, and D. Nouais, "How to measure which sort of particles was emitted earlier and which later", *Phys. Lett. B* **373** (1996) .

[5] S. Voloshin, R. Lednický, S. Panitkin, and N. Xu, "Relative space-time asymmetries in pion and nucleon production in noncentral nucleus-nucleus collisions at high-energies", *Phys. Rev. Lett.* **79** (1997) , `arXiv:nucl-th/9708044 [nucl-th]`.

[6] R. Lednický, "Femtoscopy with unlike particles", in *International Workshop on the Physics of the Quark Gluon Plasma Palaiseau, France, September 4-7, 2001.* 2001. `arXiv:nucl-th/0112011 [nucl-th]`.

[7] F. Retiere and M. A. Lisa, "Observable implications of geometrical and dynamical aspects of freeze out in heavy ion collisions", *Phys. Rev. C* **70** (2004) , `arXiv:nucl-th/0312024 [nucl-th]`.

[8] A. N. Makhlin and Yu. M. Sinyukov, "Hydrodynamics of Hadron Matter Under Pion Interferometric Microscope", *Z. Phys. C* **39** (1988) .

[9] S. V. Akkelin and Yu. M. Sinyukov, "The HBT interferometry of expanding sources", *Phys. Lett. B* **356** (1995) .

[10] A. Kisiel, "Non-identical particle femtoscopy at $\sqrt{s_{\mathrm{NN}}} = 200$ GeV in hydrodynamics with statistical hadronization", *Phys. Rev. C* **81** (2010) , `arXiv:0909.5349 [nucl-th]`.

[11] Y.-R. Liu and S.-L. Zhu, "Meson-baryon scattering lengths in HBχPT", *Phys. Rev. D* **75** (2007) , `arXiv:hep-ph/0607100 [hep-ph]`.

[12] M. Mai, P. C. Bruns, B. Kubis, and U.-G. Meissner, "Aspects of meson-baryon scattering in three and two-flavor chiral perturbation theory", *Phys. Rev. D* **80** (2009) , `arXiv:0905.2810 [hep-ph]`.

[13] W. E. Humphrey and R. R. Ross, "Low-Energy Interactions of K- Mesons in Hydrogen", *Phys. Rev.* **127** (1962) .

[14] D. Hadjimichef, J. Haidenbauer, and G. Krein, "Short range repulsion and isospin dependence in the KN system", *Phys. Rev. C* **66** (2002) , `arXiv:nucl-th/0209026 [nucl-th]`.

[15] Y. Ikeda, T. Hyodo, and W. Weise, "Chiral SU(3) theory of antikaon-nucleon interactions with improved threshold constraints", *Nucl. Phys. A* **881** (2012) , `arXiv:1201.6549 [nucl-th]`.

[16] R. Lednický and V. L. Lyuboshitz, "Final State Interaction Effect on Pairing Correlations Between Particles with Small Relative Momenta", *Sov. J. Nucl. Phys.* **35** (1982) . [Yad. Fiz.35,1316 (1981)].

[17] **ALICE** Collaboration, K. Aamodt *et al.*, "The ALICE experiment at the CERN LHC", *JINST* **3** (2008) .

[18] **ALICE** Collaboration, B. Abelev *et al.*, "Centrality determination of Pb-Pb collisions at $\sqrt{s_{NN}}$ = 2.76 TeV with ALICE", *Phys. Rev. C* **88** no. 4, (2013) , `arXiv:1301.4361 [nucl-ex]`.

[19] J. Alme *et al.*, "The ALICE TPC, a large 3-dimensional tracking device with fast readout for ultra-high multiplicity events", *Nucl. Instrum. Meth. A* **622** (2010) , `arXiv:1001.1950 [physics.ins-det]`.

[20] **ALICE** Collaboration, B. Abelev *et al.*, "Technical Design Report for the Upgrade of the ALICE Inner Tracking System", *J. Phys. G* **41** (2014) .

[21] **ALICE** Collaboration, B. Abelev *et al.*, "Performance of the ALICE Experiment at the CERN LHC", *Int. J. Mod. Phys. A* **29** (2014) , `arXiv:1402.4476 [nucl-ex]`.

[22] A. Akindinov *et al.*, "Performance of the ALICE Time-Of-Flight detector at the LHC", *Eur. Phys. J. Plus* **128** (2013) .

[23] X.-N. Wang and M. Gyulassy, "HIJING: A Monte Carlo model for multiple jet production in pp, pA, and AA collisions", *Phys. Rev. D* **44** (Dec, 1991) . `https://link.aps.org/doi/10.1103/PhysRevD.44.3501`.

[24] R. Brun, F. Bruyant, F. Carminati, S. Giani, M. Maire, A. McPherson, G. Patrick, and L. Urban, *GEANT: Detector Description and Simulation Tool; Oct 1994*. CERN Program Library. CERN, Geneva, 1993. `https://cds.cern.ch/record/1082634`. Long Writeup W5013.

[25] **ALICE** Collaboration, S. Acharya *et al.*, "Kaon femtoscopy in Pb-Pb collisions at $\sqrt{s_{NN}}$ = 2.76 TeV", *Phys. Rev. C* **96** no. 6, (2017) , `arXiv:1709.01731 [nucl-ex]`.

[26] **Particle Data Group** Collaboration, M. Tanabashi *et al.*, "Review of particle physics", *Phys. Rev. D* **98** (Aug, 2018) . `https://link.aps.org/doi/10.1103/PhysRevD.98.030001`.

[27] S. E. Koonin, "Proton Pictures of High-Energy Nuclear Collisions", *Phys. Lett. B* **70** (1977) .

[28] S. Pratt, T. Csorgo, and J. Zimanyi, "Detailed predictions for two pion correlations in ultrarelativistic heavy ion collisions", *Phys. Rev. C* **42** (1990) .

[29] G. I. Kopylov, "Like particle correlations as a tool to study the multiple production mechanism", *Phys. Lett. B* **50** (1974) .

[30] A. Kisiel, H. Zbroszczyk, and M. Szymaski, "Extracting baryon-antibaryon strong interaction potentials from p$\bar{\Lambda}$ femtoscopic correlation functions", *Phys. Rev. C* **89** no. 5, (2014) , `arXiv:1403.0433 [nucl-th]`.

[31] **ALICE** Collaboration, S. Acharya *et al.*, "p-p, p-Λ and Λ-Λ correlations studied via femtoscopy in pp reactions at $\sqrt{s}$ = 7 TeV", *Phys. Rev. C* **99** no. 2, (2019) , `arXiv:1805.12455 [nucl-ex]`.

[32] M. Chojnacki, A. Kisiel, W. Florkowski, and W. Broniowski, "THERMINATOR 2: THERMal heavy IoN generATOR 2", *Comput. Phys. Commun.* **183** (2012) , `arXiv:1102.0273 [nucl-th]`.

[33] A. Kisiel, "Non-identical particle correlation analysis in the presence of non-femtoscopic correlations", *Acta Physica Polonica B* **48** (04, 2017) .

[34] A. Stavinskiy *et al.*, "Some new aspects of femtoscopy at high energy", *Nukleonika* **49 (Supplement 2)** (2004) .
http://www.nukleonika.pl/www/back/full/vol49_2004/v49s2p023f.pdf.

[35] **ALICE Collaboration** Collaboration, K. Aamodt *et al.*, "Two-pion bose-einstein correlations in pp collisions at $\sqrt{s} = 900$ GeV", *Phys. Rev. D* **82** (Sep, 2010) .
https://link.aps.org/doi/10.1103/PhysRevD.82.052001.

[36] **ALICE** Collaboration, J. Adam *et al.*, "One-dimensional pion, kaon, and proton femtoscopy in Pb-Pb collisions at $\sqrt{s_{NN}}$ =2.76 TeV", *Phys. Rev. C* **92** no. 5, (2015) , arXiv:1506.07884 [nucl-ex].

[37] A. Kisiel, M. Gaayn, and P. Boek, "Pion, kaon, and proton femtoscopy in Pb–Pb collisions at $\sqrt{s_{NN}}$=2.76 TeV modeled in (3+1)D hydrodynamics", *Phys. Rev. C* **90** no. 6, (2014) , arXiv:1409.4571 [nucl-th].

[38] Z. Chajecki and M. A. Lisa, "Global Conservation Laws and Femtoscopy of Small Systems", *Phys. Rev. C* **78** (2008) , arXiv:0803.0022 [nucl-th].

[39] D. A. Brown, A. Enokizono, M. Heffner, R. Soltz, P. Danielewicz, and S. Pratt, "Imaging three dimensional two-particle correlations for heavy-ion reaction studies", *Phys. Rev. C* **72** (Nov, 2005) . https://link.aps.org/doi/10.1103/PhysRevC.72.054902.

[40] A. Kisiel and D. A. Brown, "Efficient and robust calculation of femtoscopic correlation functions in spherical harmonics directly from the raw pairs measured in heavy-ion collisions", *Phys. Rev. C* **80** (2009) , arXiv:0901.3527 [nucl-th].

[41] **ALICE** Collaboration, K. Aamodt *et al.*, "Two-pion Bose-Einstein correlations in central Pb-Pb collisions at $\sqrt{s_{NN}} = 2.76$ TeV", *Phys. Lett. B* **696** (2011) , arXiv:1012.4035 [nucl-ex].

[42] R. Lednický, "Finite-size effects on two-particle production in continuous and discrete spectrum", *Phys. Part. Nucl.* **40** (2009) , arXiv:nucl-th/0501065 [nucl-th].

A Stavinskiy reference method

Another option for obtaining the reference distribution, $B(k^*)$, is to use, what will be referred to as, the "Stavinskiy method" [34]. The method was first proposed to handle the case of one event femtoscopy, and has been suggested for use in eliminating momentum conservation effects in the reference distribution [1]. The method is appropriate for collisions between symmetric projectiles, at sufficiently large energy, with a detector which is symmetrical with respect to the ~~transition~~ transformation $\mathbf{r} \to -\mathbf{r}$. The use of this method in a three-dimensional analysis of two-pion correlations produced, in comparison to the event mixing results, an increase of 6% for R_{side} at low-k_{T} and up to 4% for R_{out} and R_{long} [41]. The purpose of using the Stavinskiy method in this ΛK analysis is to rid the correlation functions of the non-femtoscopic background. More specifically, the intent is to handle background contributions from elliptic flow, and other sources having reflection symmetry in the transverse plane. With the Stavinskiy method, mixed-event pairs are not used for the reference distribution; instead, same-event pseudo-pairs, formed by rotating one particle in a real pair by 180° in the transverse plane, are used [35]. This rotation rids the pairs of any femtoscopic correlation, while maintaining correlations due to elliptic flow (and other suitably symmetric contributors). Care needs to be taken in treating the pseudo-pairs exactly like the real pairs; e.g., the pseudo-pairs should be exposed to the same pair rejection procedures used in the analysis on the real pairs. The results of correctly implementing such a procedure are shown in Fig. A.1. The figure demonstrates, for the ΛK$^+$ system, that the Stavinskiy method is effective in flattening the correlation function in the region where no femtoscopic signal is expected. This procedure flattens the non-femtoscopic background equally well for the ΛK$^-$ system, but is less effective for the ΛK$_{\mathrm{S}}^0$ system.
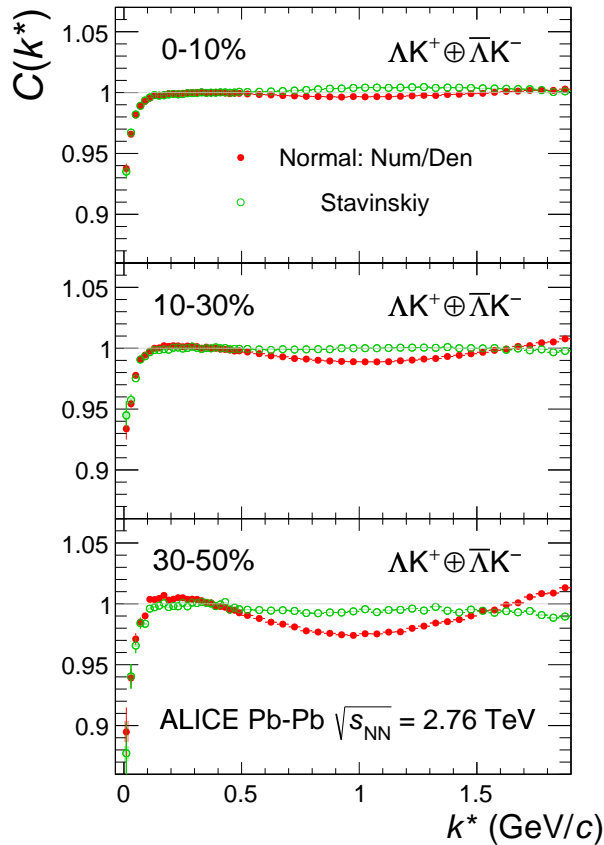

Figure A.1: (Color online) Correlation functions for the ΛK$^+ \oplus \overline{\Lambda}K^-$ system built using the Stavinskiy method for 0–10%, 10–30%, and 30–50% centrality intervals. Closed symbols represent correlations built using the normal mixed-event reference distribution, while open symbols represent correlations formed using the Stavinskiy same-event pseudo-pairs as a reference.

B Strong and Coulomb fitter

When modeling systems which include both strong and Coulomb effects, Eq. ~~5~~ (5) is no longer valid, and there exists no analytical form with which to fit. To model such a system, a more fundamental approach must be taken, beginning with Eq. ~~2~~ (2) and using the two-particle wave-function which includes both strong and Coulomb interactions [42],

$$\Psi_{\mathbf{k}^*}(\mathbf{r}^*) = e^{i\delta_c}\sqrt{A_c(\eta)}[e^{i\mathbf{k}^*\cdot\mathbf{r}^*}F(-i\eta,1,i\xi) + f_c(k^*)\frac{\tilde{G}(\rho,\eta)}{r^*}], \tag{B.1}$$

where $\rho = k^*r^*$, $\eta = (k^*a_c)^{-1}$, $\xi = \mathbf{k}^*\cdot\mathbf{r}^* + k^*r^* \equiv \rho(1+\cos\theta^*)$, and $a_c = (\mu z_1 z_2 e^2)^{-1}$ is the two-particle Bohr radius (including the sign of the interaction). Furthermore, δ_c is the Coulomb s-wave phase shift, $A_c(\eta)$ is the Coulomb penetration factor, $\tilde{G} = \sqrt{A_c}(G_0 + iF_0)$ is a combination of the regular (F_0) and singular (G_0) s-wave Coulomb functions. Finally, $f_c(k^*)$ is the s-wave scattering amplitude,

$$f_c(k^*) = \left[\frac{1}{f_0} + \frac{1}{2}d_0 k^{*2} - \frac{2}{a_c}h(\eta) - ik^* A_c(\eta)\right]^{-1}, \tag{B.2}$$

where the "h-function", $h(\eta)$, is expressed through the digamma function, $\psi(z) = \Gamma'(z)/\Gamma(z)$ as

$$h(\eta) = 0.5[\psi(i\eta) + \psi(-i\eta) - \ln(\eta^2)]. \tag{B.3}$$

In this case, the λ parameter may be included as

$$C(\mathbf{k}^*) = (1-\lambda) + \lambda \int S(\mathbf{r}^*)|\Psi_{\mathbf{k}^*}^S(\mathbf{r}^*)|^2 \underline{d}\underline{d}^3\underline{\mathbf{r}^*}\underline{r^*}. \tag{B.4}$$

To build a fit function for a system including both strong and Coulomb interactions two related options were considered. The first option was to numerically integrate Eq. ~~2~~(2). The second option was to simulate a large sample of particle pairs, calculate the wave function describing the interaction, and average to obtain the integral in Eq. ~~2~~(2). For this analysis, the latter option was adopted.

C Relative emission shifts with THERMINATOR 2

Figure C.1 shows ΛK^+ results from the THERMINATOR 2 event generator for an impact parameter of $b = 2$ fm. As THERMINATOR 2 does not include any final state effects, the femtoscopic correlation was introduced by assuming a set of scattering parameters ($\Re f_0$, $\Im f_0$, $d_0) = (-0.60$ fm, 0.51 fm, 0.83 fm) and weighting the ~~signal distribution (numerator pairs)~~ pairs in the signal distribution with the modulus squared of the two-particle wave function, $|\Psi|^2$.

The top row of Fig. C.1 shows the experimental $\Lambda K^+ \oplus \overline{\Lambda}K^-$ data together with the simulation results (a) for the one-dimensional correlation function and (b) for the real part of the $l = 1$, $m = 1$ component, $\Re C_{11}$, of the spherical harmonic decomposition. The other four plots in Fig. C.1 show the two-particle emission function (i.e., the pair separation distributions) from the simulation in the (c) out (r^*_{out}), (d) side (r^*_{side}), and (e) long (r^*_{long}) directions, as well as (f) the temporal characteristics of the source (Δt^*), all measured in the PRF. The source distributions have all been fitted with a Gaussian form, the results of which are printed within the respective plots. One immediately sees a significant spatial shift in the out direction, $\mu_{\text{out}} \approx 4$ fm, and negligible shift in the other two directions, $\mu_{\text{side}} \approx \mu_{\text{long}} \approx 0$ fm. In other words, the figure demonstrates that, within the THERMINATOR 2 model, the Λ is, on average, emitted further out than its K partner. Additionally, the figure shows a nonzero temporal shift, $\mu_{\Delta t} \approx -2.7$ fm/c, signifying that the Λ is, on average, emitted earlier than its K partner within the model.

This section concludes with a brief look at how a spatial separation of the single particle sources affects the radii extracted from a femtoscopic analysis. To achieve this, THERMINATOR 2 is used in a similar
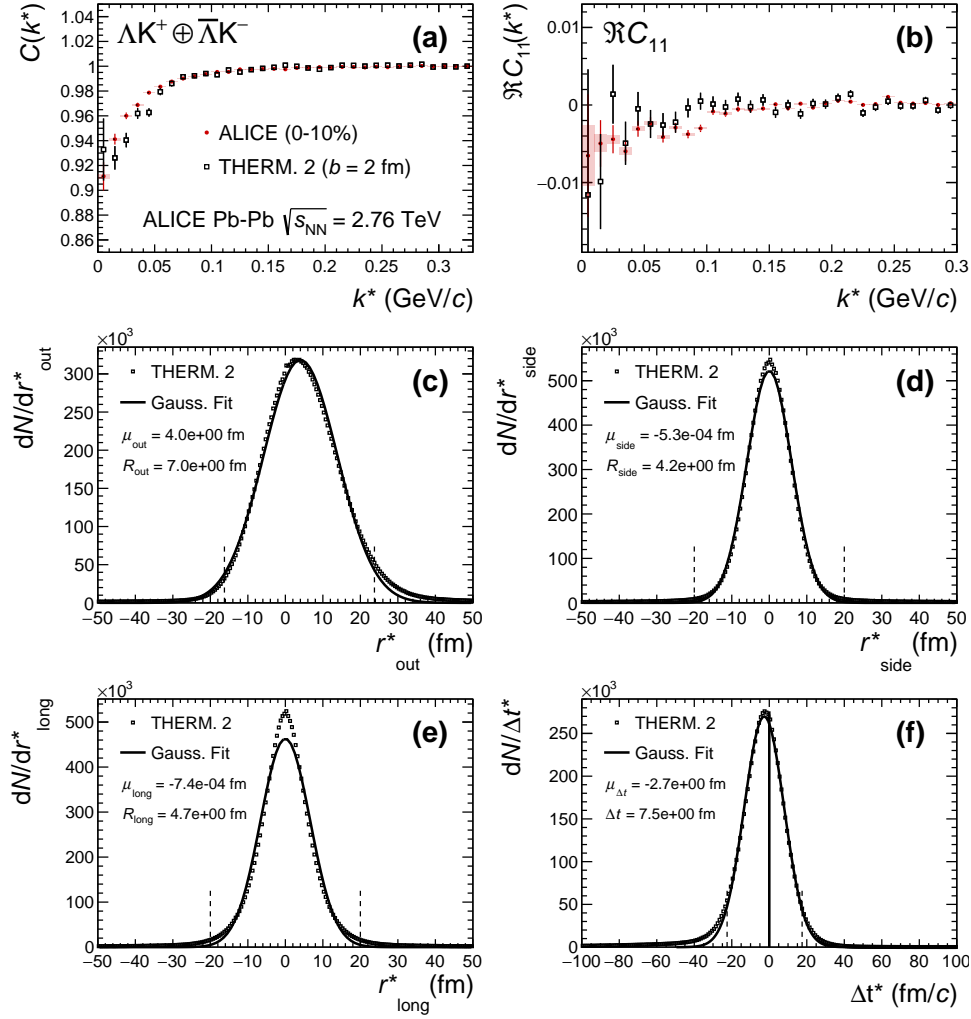
Figure C.1: Results from the THERMINATOR 2 simulation implemented with an impact parameter $b = 2$ fm for the $\Lambda\mathrm{K}^+$ pair system. (a) the one-dimensional correlation function from THERMINATOR 2 together with the experimental data. (b) the $\Re C_{11}$ component of a spherical harmonic decomposition of the THERMINATOR 2 simulation together with the experimental data. The other four panels show the source distribution from the simulation in the (c) out, (d) side, and (e) long directions, as well as (f) the temporal characteristics, all in the PRF. The source distributions have all been fitted with a Gaussian form over the regions contained within the dashed lines, the results of which are printed within the respective plots.

fashion as described above, but with one important difference. Instead of taking the source information from THERMINATOR 2, the source is drawn from a pre-determined Gaussian distribution. In all, $R_{\mathrm{out}} = R_{\mathrm{side}} = R_{\mathrm{long}} = 5$ fm, and $\mu_{\mathrm{side}} = \mu_{\mathrm{long}} = 0$ fm. The cases of $\mu_{\mathrm{out}} = 0$ fm, $\mu_{\mathrm{out}} = 1$ fm, $\mu_{\mathrm{out}} = 3$ fm, and $\mu_{\mathrm{out}} = 6$ fm were studied within the simulation. Note, within this implementation there is no time difference in the emission of the Λ and K particles. For each, a one-dimensional correlation function is generated and fit with the Lednický model, as shown in Fig. C.2. The scattering parameters are known precisely here, as they served as the weights used in the simulation, and are kept constant in the fit. Only the extracted one-dimensional source size is of interest here, so the λ parameter is also fixed at unity. The figure demonstrates that as the separation μ_{out} increases, so do the extracted femtoscopic radii. Figure C.3 shows, together with the experimental $\Lambda\mathrm{K}^+$ data, the effect of increasing μ_{out} on the spherical harmonic $l = 0$, $m = 0$ component, C_{00}, and on the real part of the $l = 1$, $m = 1$ component, $\Re C_{11}$. The figures shows that as μ_{out} increases, so does the magnitude of the $\Re C_{11}$ signal.
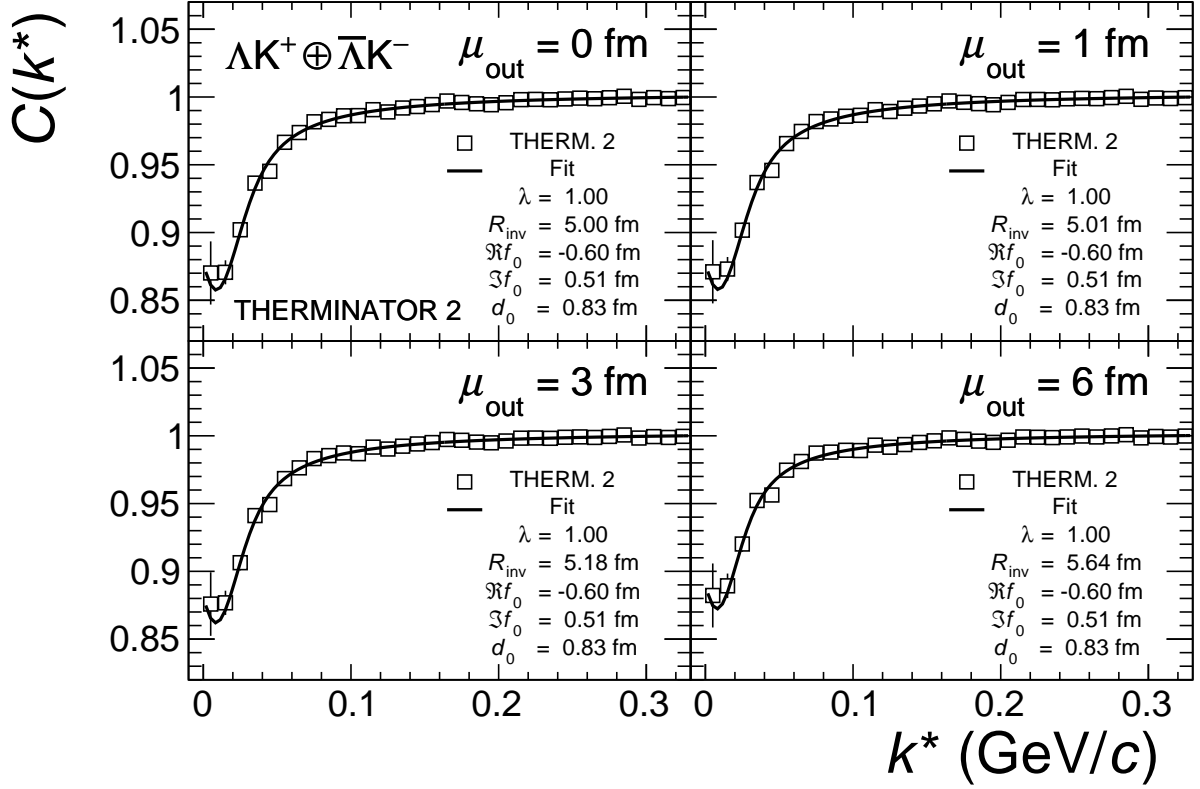
Figure C.2: Probing the effect of varying the source shift in the outward direction, μ_{out}, within the THER-MINATOR 2 framework. To achieve this, particle pairs are formed from the simulation, but with altered spatial characteristics achieved by drawing the out, side, and long components from predetermined Gaussian distributions. The sources in all three directions are Gaussians of width 5 fm. The distributions used for the side and long direction are centered at the origin, while the shift in the outward direction, μ_{out}, is varied. The plots show fits resulting from sources with μ_{out} increasing from 0 to 6 fm. The effect of increasing μ_{out} clearly increases the effective radius extracted in the fit.
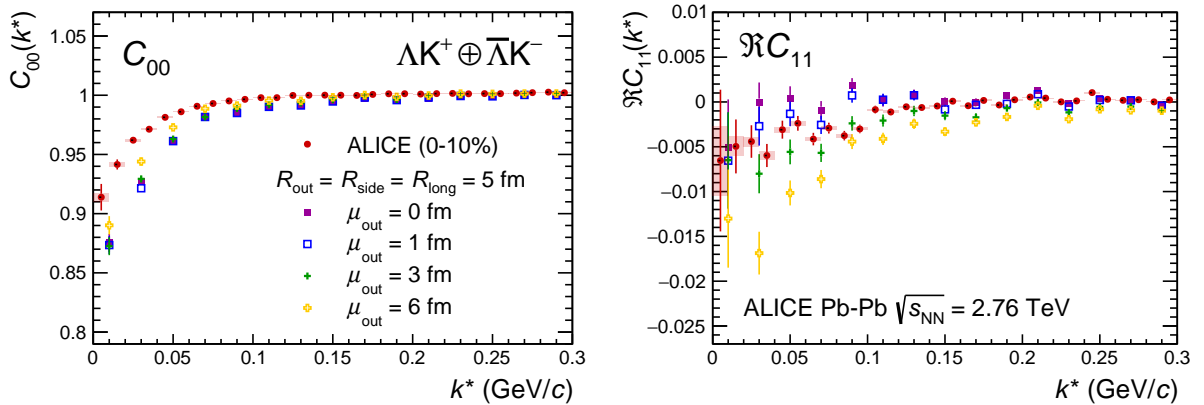

Figure C.3: (Color online) Spherical harmonics components (left) C_{00} and (right) $\Re C_{11}$ of the ΛK^+ correlation function for the 0–10% centrality interval shown with results from the THERMINATOR 2 simulation implemented with different shifts in the outward direction, μ_{out}, as described in the text.

728 **D   The ALICE Collaboration**